

Quantum-Chemical Calculations of Transition-Metal Oxynitrides

Von der Fakultät für Mathematik, Informatik und Naturwissenschaften der
Rheinisch-Westfälischen Technischen Hochschule Aachen zur Erlangung des
akademischen Grades eines Doktors der Naturwissenschaften
genehmigte Dissertation

vorgelegt von

Diplom-Chemiker
Marck-Willem Lumey

aus Heerlen (NL)

Berichter: Universitätsprofessor Dr. R. Dronskowski
Universitätsprofessor Dr. U. Simon

Tag der mündlichen Prüfung: 30.01.2006

Diese Dissertation ist auf den Internetseiten der Hochschulbibliothek online verfügbar

If one does not fail at times,
then one has not challenged himself.

Ferdinand Porsche

Parts of this work are already published or submitted for publication:

M.-W. Lumey and R. Dronskowski

The Electronic Structure of Tantalum Oxynitride and the Falsification of
 α -TaON

Z. Anorg. Allg. Chem., **629** (2003) 2173

M.-W. Lumey and R. Dronskowski

Quantum-Chemical Studies on the Geometric and Electronic Structures of
Bertholloide Cobalt Oxynitrides

Adv. Funct. Mater., **14** (2004) 371

M.-W. Lumey and R. Dronskowski

First-Principles Electronic Structure, Chemical Bonding, and High-Pressure
Phase Prediction of the Oxynitrides of Vanadium, Niobium and Tantalum

Z. Anorg. Allg. Chem., **631** (2005) 887

T. Bredow, M.-W. Lumey, R. Dronskowski, H. Schilling, J. Pickardt, M. Lerch

Structure and Stability of TaON Polymorphs

Z. Anorg. Allg. Chem., submitted

Contents

1. Introduction	1
2. Electronic Structure Calculations	3
2.1 Density-Functional Theory	4
2.2 Exchange and Correlation Functionals	6
2.3 Applied Density-Functional Methods	7
2.3.1 Pseudopotentials	7
2.3.2 Augmented Plane Wave (APW)	8
2.3.3 Linearized Augmented Plane Wave (LAPW)	10
2.3.4 Linearized Muffin-Tin Orbital (LMTO)	11
2.3.5 Bonding analysis: COHP	12
3. Binary Oxides and Nitrides of the First-Row Transition Metals	14
3.1 First-Row Transition-Metal Oxides	15
3.2 First-Row Transition-Metal Nitrides	20
4. Oxynitrides of the 3d Transition Metals	25
4.1 3d Transition-Metal Oxynitrides; Structure and Magnetism . . .	26
4.2 Thermodynamic Stability	32
4.3 Supercell Stoichiometry	34
5. Oxynitrides of Vanadium, Niobium and Tantalum	39
5.1 Stoichiometrically Precise Vanadium Oxynitride	40
5.2 Niobium Oxynitride	47
5.3 Tantalum Oxynitride	50
5.3.1 β -TaON	54

5.3.2	α -TaON	57
5.3.3	Discussion	62
5.3.4	Mixed Oxynitrides of Niobium and Tantalum	63
5.3.5	High-pressure phases of NbON and TaON	65
5.3.6	Anion order in VON, NbON and TaON	70
6.	Summary	73
	Bibliography	76
A.	Technical Details	84
A.1	LMTO	84
A.2	Wien2k	84
A.3	VASP	84
A.4	wxDragon	85
B.	Crystal Data	86
C.	Results on VON	87
D.	Results on high-pressure phases of TaON	89

List of Tables

1	Experimental properties of the binary transition-metal oxides and nitrides.	14
2	Calculated energies of the the $3d$ transition-metal oxides in different spin-orientations	16
3	Experimental and calculated band gaps for MnO, FeO, CoO and NiO in the rocksalt structure.	17
4	Calculated and experimental formation enthalpies of the $3d$ transition-metal oxides.	19
5	Calculated energies of the the $3d$ transition-metal nitrides in different spin-orientations	21
6	Calculated energies (eV/f.u.) of the supercell structures with different anion arrangements of the $3d$ transition-metal oxynitrides.	35
7	Properties of several hypothetical polymorphs of VON	41
8	Comparison of the energies and volumes of the educts ($V_2O_5 + 3 VN + N_2$) and products (5 VON in several different structure types)	45
9	Experimental and theoretical structure data of NbON on the basis of pseudopotential-GGA calculations.	48
10	Theoretical total energies and volumes of NbON as a function of anionic ordering on the basis of pseudopotential-GGA calculations	49
11	Experimental and theoretical structure data of β -TaON on the basis of pseudopotential-GGA calculations.	54

12	Theoretical total energies of α -TaON (lattice parameters fixed) as a function of anionic ordering on the basis of pseudopotential-GGA calculations.	57
13	Experimental and theoretically optimized volumes/energies for α -TaON on the basis of pseudopotential-GGA calculations. . . .	58
14	Energy of the niobium substituted tantalum oxynitrides in comparison with the simple ternary compounds, TaON and NbON.	64
15	Properties of several hypothetical polymorphs of TaON.	66
16	Theoretical relative energies as a function of anionic ordering for VON, NbON and TaON.	70
17	ICOHP values for the N–N, N–O and O–O bonds of VON in the baddeleyite structures for different anion arrangements.	72
18	Experimental and calculated properties of 3d transition-metal nitrides and oxides.	86
19	Properties of all calculated hypothetical polymorphs of VON	87
20	Properties of all calculated high-pressure hypothetical polymorphs of TaON.	89

List of Figures

1	The partition of a unit cell in localized and interstitial regions	9
2	Schematic drawing of the APW and LAPW method	10
3	Differences between the theoretical and experimental formation enthalpy	20
4	Experimental and calculated volumes for the $3d$ transition-metal nitrides.	23
5	Energy difference between the $3d$ transition-metal oxynitrides in the rocksalt and the zinc blende type, for the nonmagnetic case.	26
6	Electronic structure of $\text{CrO}_{0.5}\text{N}_{0.5}$ in the lowest-energy rocksalt type structure.	27
7	Electronic structure of $\text{CrO}_{0.5}\text{N}_{0.5}$ in the lowest-energy zinc blende type structure.	28
8	Crystal Orbital Hamilton Populations (COHP) for the Cr–Cr interactions of $\text{CrO}_{0.5}\text{N}_{0.5}$ in the rocksalt and the zinc blende type	29
9	Energy difference between the $3d$ transition-metal oxynitrides in the rocksalt and the zinc blende type.	31
10	Formation energy of the $3d$ transition-metal oxynitrides relative to the binary oxides and nitrides.	33
11	Supercell containing $2 \times 2 \times 2$ conventional cubic cells of the zinc blende structure of $\text{CoO}_{0.5}\text{N}_{0.5}$	35
12	Radial distribution function (RDF) of the Co–N and Co–O interatomic distances in the $\text{CoO}_{0.5}\text{N}_{0.5}$	36
13	Theoretical ΔE -x diagram calculated for various $\text{CoO}_x\text{N}_{1-x}$ compositions according to Equation 1.	37

14	Energy-volume diagram of VON with four baddeleyite-related structures.	42
15	Coordination of vanadium for the high-pressure monoclinic structure and the distorted baddeleyite structure.	43
16	Unit cell of vanadium oxynitride in the regular and distorted baddeleyite structure.	44
17	Theoretical enthalpy-pressure diagram for VON.	46
18	Density-of-states of VON in the baddeleyite structure with local $3d$ projections and crystal orbital Hamilton populations (COHP)	47
19	Electronic structure of NbON in the baddeleyite structure, calculated with the TB-LMTO-ASA method using the LDA.	49
20	The mono-capped TaO_3N_4 prisms within the β -TaON structure.	51
21	Crystal structures for α -TaON derived from single crystals	53
22	Band structure, density-of-states (DOS), and Crystal Overlap Hamilton Population (COHP) in β -TaON.	56
23	Energetically mostly favored anionic arrangement calculated for α -TaON on the basis of pseudopotentials and the GGA.	59
24	Theoretical density-of-states (DOS) of α -TaON, including tantalum, nitrogen and oxygen projections in black, on the basis of FLAPW and the GGA.	60
25	Experimentally reported diffraction diagram of α -TaON using $\text{Cu-K}\alpha_1$ radiation and simulated diffraction diagram.	61
26	Band structure of $\text{Ta}_2\text{Nb}_2\text{O}_4\text{N}_4$ in the baddeleyite structure and density-of-states with the tantalum and niobium projections.	65
27	Calculated energy-volume diagram of TaON in different structure types.	67
28	Theoretical enthalpy-pressure diagram of TaON.	67
29	Tantalum coordination in the high-pressure cotunnite structure of TaON, a distorted trigonal prism capped on all rectangular faces.	68
30	Density-of-states of TaON in the cotunnite structure with local $3d$ projections and Crystal Orbital Hamilton Populations (COHP) for the Ta-Ta, Ta-O and Ta-N interactions.	69

1. Introduction

For many years the search for novel solid-state materials was dominated by investigations on oxides. Within the last decades, however, this has more shifted towards carbides and nitrides. A recent development is to combine these binary archetypical compounds in the form of carbonitrides and oxynitrides. The major idea behind this approach is to combine the properties of both binary single classes and show that these mixed ternary compounds exhibit new chemical and physical properties and thus allow for exciting applications. For example, technological use of oxynitrides has first been discovered in the fields of ionic conductivity and also bifunctional catalysis [1–3]. Moreover, oxynitrides containing transition metals are already under production as novel inorganic pigments, thereby replacing traditional toxic materials which typically contain cadmium [4]. Very recently, perovskite-type oxynitrides have been developed which may lead to new thermoelectrics for high-temperature solar generators [5]. Despite these commercial applications, the majority of the oxynitride investigations may be looked upon as fundamental research. This research is mainly characterized by the quite elaborated synthesis of oxynitride compounds using very advanced techniques, e.g. CVD (Chemical Vapor Deposition), Sputtering and PLD (Pulsed Laser Deposition). These expensive techniques indicate that the synthesis of oxynitrides is not that simple and that many of the oxynitrides may be even metastable with respect to the educts. Also, questions about the oxygen-nitrogen distribution, ordering and stoichiometry are difficult to solve with X-ray techniques. This originates from the fact that N^{3-} and O^{2-} are isoelectronic and therefore hard to distinguish with this method. Theoretical investigations can answer some of these unsolved questions especially since only *one* device has to be used: *the computer*. In this work parts of the problems will

be solved using density-functional techniques.

First, a general investigation on the $3d$ transition-metal oxynitrides will be presented. The emphasis is placed on the structure and stability of these oxynitrides. The experimentally synthesized cobalt oxynitride was picked for a more detailed look on anion order and stoichiometry, possibly leading to the first magnetic oxynitride.

In addition, the oxynitrides of the fifth group (V, Nb and Ta) are explored. Tantalum oxynitride is used as a pigment due to its bright yellow color and is probably therefore one of the most investigated transition-metal oxynitride. Moreover, it exhibits one specific anion order. A second peculiar phase of TaON is listed in the inorganic crystal structure database (ICSD, [6]), and it will be studied whether or not its existence is supported by electronic-structure theory. Niobium oxynitride adopts the same structure type as tantalum oxynitride and might also have the same anion order, but it is colored in blue. Since the color depends on the band gap of the solid, the latter being a function of ionicity and covalency, theoretical calculations are ideally suited to better understand the electronic and optical properties of these compounds. Until now, vanadium oxynitrides are only known as non-stoichiometric compounds adopting the rocksalt structure-type. A stoichiometrically precise vanadium oxynitride has not been synthesized yet. Theoretical investigations will predict the first high-pressure synthesis of VON and give detailed information about its structural and electronic properties. This work is a theoretical start of the fundamental research of transition-metal oxynitrides and it tries to illuminate the path leading to the carefully directed synthesis of new oxynitrides for novel future applications.

2. Electronic Structure Calculations

In 1666 Newton started with his famous work (*Philosophiae Naturalis Principia Mathematica*) about mechanics and gravitation, which was published in 1687 [7]. This was the beginning of the mathematical description of the motion of celestial bodies. Many other scientists extended and enhanced Newton's primal investigations, leading to an excellent description of our macroscopic world. In 1887 the great chemist Berthelot even wrote "from now on there is no mystery about the universe". At the end of the 19th century, however, the classical theory failed to explain several experiments concerning the microscopic world of atoms and molecules. These contradictions opened the path for a new theory: the quantum theory, which was mainly developed by Planck, Einstein, Bohr and Heisenberg [8]. It was Schrödinger, back in 1926, who combined the classical Hamiltonian approach with the Fermat principle of light, resulting in his great discovery, Schrödinger's wave equation [9]. Nowadays Schrödinger's equation forms the basis of almost every electronic-structure calculation. During the last decades, several different attempts have been developed to solve this equation. These approaches can be divided into two main groups. On the one side, there exist empirical methods which use several assumptions and parameterizations but provide in many cases good results and gain solid insights into the calculated system. On the other side, there are the *ab initio* (Lat.: from the beginning) methods, without any approximations at all, except for the Born–Oppenheimer approximation which is applied in both particular methods. It states that the movements of the lighter and therefore more mobile electrons may be studied in an environment of prefixed nuclei. This is equivalent with studying the motions of the electrons and nuclei separately. In this work the density-functional theory (DFT) is used which is usually looked upon as being part of the *ab initio* meth-

ods. DFT is a ground-state theory and can therefore not be used for calculation of excited states. Even when band gaps of semiconductors are often calculated correctly, this has no physical background. A more detailed description of this particular method is given in the subsequent sections.

2.1 Density-Functional Theory

Traditional methods in electronic structure theory like Hartree–Fock theory are based on the complicated many-electron wavefunction. The main objective of density-functional theory is to replace the many-body electronic wavefunction by the electronic density as the basic quantity. The first true density-functional theory was developed by Thomas and Fermi in the late 1920s [10, 11]. They calculated the energy of an atom by representing its kinetic energy as a functional of the electron density, combining this with the classical expressions for the nuclear-electron and electron-electron interactions (which can both also be represented in terms of the electron density). The reader should remind that the Hartree–Fock method (1930) was developed almost simultaneously. Another early density-functional theory was proposed by Slater who constructed the so-called $X\alpha$ method where a one-parameter approximate exchange functional was used [12]. Although density-functional theory has its conceptual roots in the Thomas–Fermi model, DFT was not put on a firm theoretical footing until the Hohenberg–Kohn theorem was proposed in 1964 [13]. They demonstrated that the total energy of a system of interacting electrons is an exact functional of the electron density:

$$E_{\text{tot}} = E_{\text{tot}}[\rho] \quad (1)$$

Further they proved that the minimum value of the total-energy functional is the ground-state energy of the system, and the density that yields this minimum value is the exact ground-state density (ρ_0),

$$E_{\text{tot}}[\rho_0] \leq E_{\text{tot}}[\rho] \quad (2)$$

The Hohenberg–Kohn theorem is only an existence theorem, stating that the mapping exists, but it does not provide any such exact mapping. It is in these

mappings where approximations are made. One problem which arises is to find the proper total-energy functional. Kohn and Sham approximated the solution to this problem by decomposing the total energy into the following form [14]:

$$E_{\text{tot}}[\rho] = E_{\text{nn}}[\rho] + E_{\text{en}}[\rho] + E_{\text{ee}}[\rho] + T[\rho] + E_{\text{xc}}[\rho], \quad (3)$$

where $E_{\text{nn}}[\rho]$, $E_{\text{ee}}[\rho]$ and $E_{\text{en}}[\rho]$ are the Coulomb interactions between the nuclei, the electrons and the nuclei and the electrons respectively. $T[\rho]$ is the kinetic energy of the non-interacting particles and $E_{\text{xc}}[\rho]$ is the so-called exchange-correlation energy. This latter term contains all the other electron-electron contributions which are not properly covered by the Coulomb interactions.

Within the framework of Kohn–Sham DFT, the intractable many-body problem of interacting electrons in a static external potential is reduced to a tractable problem of non-interacting electrons moving in an effective potential (V_{eff}). The effective potential includes the effects of the Coulomb interactions between the electrons and the exchange-correlation term and is due to the minimization of the total energy with respect to the electron density defined as,

$$V_{\text{eff}} = \frac{\delta E_{\text{nn}}}{\delta \rho} + \frac{\delta E_{\text{en}}}{\delta \rho} + \frac{\delta E_{\text{ee}}}{\delta \rho} + \frac{\delta E_{\text{xc}}}{\delta \rho} \quad (4)$$

The wavefunction of the non-interacting electrons can be obtained by solving the single-electron Kohn–Sham equation using V_{eff} ,

$$[\hat{T} + V_{\text{eff}}]\psi_i(r) = \epsilon_i \psi_i(r), \quad (5)$$

where ψ_i is a one-electron wavefunction of the electronic state i and ϵ_i the corresponding Kohn–Sham eigenvalue. The solution of the Kohn–Sham equations would be exact if the exchange-correlation within the V_{eff} term could be correctly described. Nonetheless approximations have to be made, and the most common is the local-density approximation (LDA) which gives an approximate mapping from the density of the system to the total energy. The LDA is exact for the uniform electron gas. The electronic density is given by

$$\rho(r) = \sum_{i=1}^N |\psi_i(r)|^2. \quad (6)$$

Thus we can get V_{eff} through the initial electronic density and find $\psi_i(r)$ from the Kohn–Sham equation (Equation 5). Given that $\psi_i(r)$, a new electronic density can be calculated according to Equation 6. Consequently, the Kohn–Sham scheme naturally leads to an iterative procedure where the electronic density is refined through a self-consistency cycle.

2.2 Exchange and Correlation Functionals

The correct description of the exchange and correlation energies is the central problem within density-functional theory. The simplest method, as proposed by Kohn and Sham [14], is the local-density approximation. In the local-density approximation the exchange-correlation energy of the investigated system is assumed to be the same as the exchange-correlation energy of a homogeneous electron gas ($\epsilon_{\text{xc}}^{\text{hom}}(r)$) with the same density.

$$E_{\text{xc}}^{\text{LDA}}[\rho] = \int \epsilon_{\text{xc}}^{\text{hom}}(r)\rho(r)dr \quad (7)$$

Within the LDA, there exist several parameterizations for the exchange-correlation energy of the homogeneous electron gas, for example the one from von Barth and Hedin [15], which is used in most LMTO calculations. It is therefore astonishing that, despite these crude approximations, in many cases the local-density approximation gives quite satisfactory results, particularly in systems with a slowly varying electron density. This can be partly attributed to a correct description of the exchange-correlation hole within the local-density approximation.

In strongly correlated systems the LDA approach is not sufficient anymore and strong interelectronic correlation may be included by adding an empirical energy U to the LDA scheme (LDA+ U method). Alternatively, gradient corrections can be taken into account as it has been done in the generalized gradient approximation (GGA) for which we used the parameterizations of Perdew and Wang [16]. The GGA approach is actually only a gradient correction of the LDA method:

$$E_{\text{xc}}^{\text{GGA}}[\rho] = \int F(\rho(r), \nabla\rho(r))dr \quad (8)$$

It may be generally said that LDA calculations typically result in too short lattice parameters which can be attributed to an overbinding of the atoms. On the other side, the GGA approach results in a slight overestimation of the lattice parameters. Moreover, the magnetic properties and the magnetic moments particularly are underestimated within the LDA method.

2.3 Applied Density-Functional Methods

The general theoretical background of DFT and its major approximations were explained in the previous section. In this section the practical use of density-functional theory will be illustrated. The application of DFT into the solid state requires the implementation of the translational symmetry (Bloch's theorem) which has major consequences for the choice of the used basis set. Generally the used programs can be divided into three different approaches concerning this treatment of the basis set. On the one side one may prefer delocalized orbitals (e.g., plane waves) which are perfectly adapted to the periodic boundary conditions and Bloch's theorem. On the other side one may use localized atomic orbitals, which provide a comfortable insight into the observed system, since the interpretation of the electronic wavefunctions in terms of atomic wavefunctions is straightforward. Alternatively one can use a combination of both types of basis functions.

2.3.1 Pseudopotentials

The use of a plane-wave basis is properly the most natural basis set for solid state calculations. The major disadvantage of a pure plane-wave approach is that the correct description of the strong oscillations of the wavefunctions close to the nucleus require a superposition of plenty of plane waves. This, however, is a very resource-consuming procedure and not suitable for common quantum chemistry calculations. In order to simplify the strong oscillations of the wavefunction close to the nucleus, they are substituted by a much smoother pseudo wavefunction. This is accomplished by a substitution of the true potential inside the core by a suitable pseudopotential. This pseudopotential replaces the strong

interactions of the valence electrons with the inner electrons and with the nuclei. The atoms can hereby regarded as perturbations in a plane-wave expansion. Many choices of pseudopotentials are possible and they are generated from first-principles calculations. The art is to find a pseudopotential which is both soft and transferable. A soft pseudopotential generates pseudo-wavefunctions which are flat near the nuclei, such that they can be described by only a few plane waves. A pseudopotential is called transferable if it gives the correct physical behavior of the valence electrons in any chemical environment. The quality of the calculations can be improved by increasing the kinetic energy cut-off of the plane waves. On the one side, this higher cut-off leads to a better description of the strong oscillations of the wavefunction close to the nucleus, but on the other hand many more plane waves are required to achieve this, which leads inevitably to an increase of computational resources. In our specific cases, an energy cut-off of 500 eV was sufficient.

The theoretical background of VASP [17–22] is based on this plane-wave/pseudopotential approach and the program was mainly used for the relaxation of novel compositions in known structure types. The relaxation of the atoms and unit cells into their ground-state can be performed because the forces and stress tensors can easily be calculated. The main goal hereby was to identify new materials and setting up an appropriate high-pressure synthesis. More technical details about the used methods are listed in Appendix A.

2.3.2 Augmented Plane Wave (APW)

The idea behind the augmented plane-wave method is quite similar to the one of the pseudopotential approach. In the region between the atoms, far away from the nuclei, the electrons can move more or less freely and they are described by plane waves. This region is called interstitial region (II). The electrons close to the nuclei, however, are described by atom-like functions, instead of pseudopotentials. They are located within so-called muffin-tin spheres around the atoms (A,B, region I) in the unit cell. The partition of the unit cell is illustrated in Figure 1.

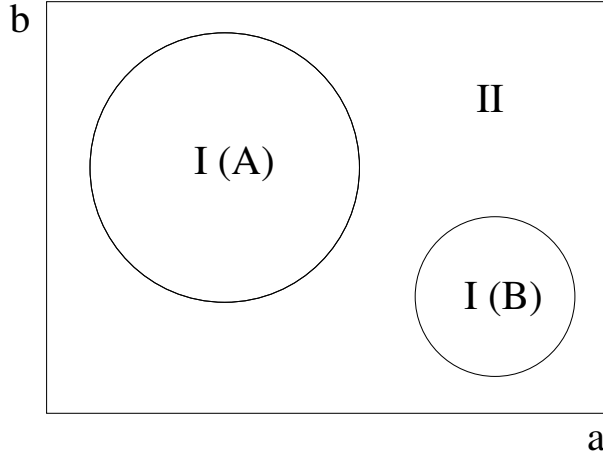


Figure 1: The partition of a unit cell in two regions is indicated. The circles (region I) show the muffin-tin spheres around the atoms A and B, where region II fills the interstitial space.

There are several ways to solve the Kohn–Sham equations within these regions and this has led to several different methods (APW [23], KKR [24, 25], MTO [26]). Essentially they are all based on the same approach of dividing the wavefunction into a part inside the muffin-tin (MT) sphere (region I) and one outside the MT-sphere (region II). Within the APW approach, the composite wavefunction consists of atomic functions for region I and a plane wave for region II, as is illustrated by Equation 9.

$$\begin{aligned}
 \phi_{k_n} &= \sum_{lm} c_{lm,k_n} R_{k_n,l}(r) Y_l^m(\vartheta, \varphi) & r < R_{\text{MT}} \\
 &= e^{ikr} & r \geq R_{\text{MT}}
 \end{aligned} \tag{9}$$

The first part of Equation 9 is simply a linear combination of radial functions ($R_{k_n,l}(r)$) times the spherical harmonics ($Y_l^m(\vartheta, \varphi)$) and describes the strong oscillating atomic orbitals in region I. For the smoother part of the wavefunction, a plane-wave expansion is used (second part of equation). The major difficulty is to find out how the borderline between the regions I and II is properly dealt with. At the muffin-tin radius, the inner wavefunctions are augmented by outer wavefunctions, schematically plotted in Figure 2 [27].

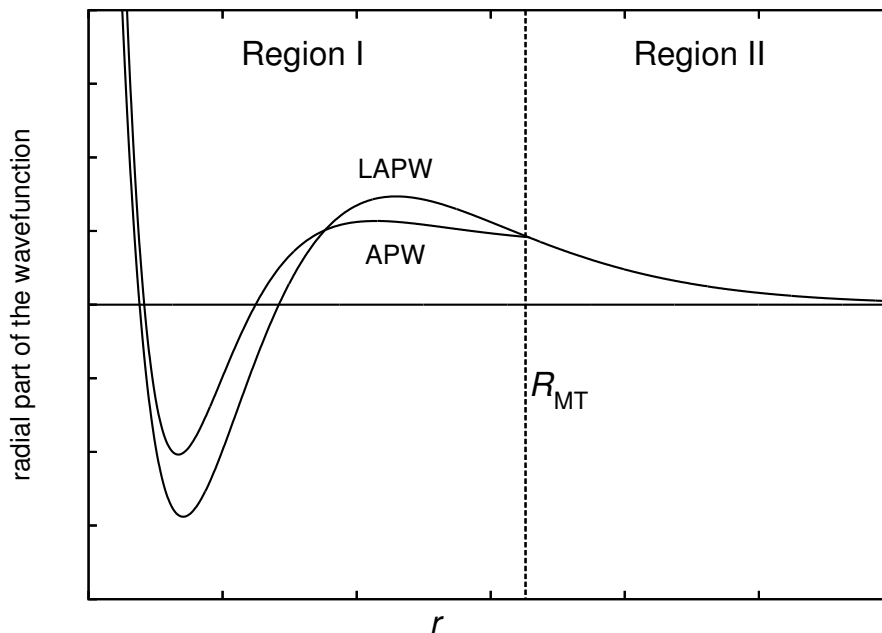


Figure 2: Schematic drawing of the augmentation process at the muffin-tin border utilized in the APW and LAPW method.

In the APW approach, these energy dependent wavefunctions do not have to be differentiable at the border, but in that case, the computational effort to solve the Kohn–Sham matrix is enormous. The solution is found in the linear methods (LMTO and LAPW) [28].

2.3.3 Linearized Augmented Plane Wave (LAPW)

The linearization of the APW method guarantees a differentiable wavefunction because it requires that at the border of the two regions the function in the sphere matches the plane wave both in value and slope. Moreover only one diagonalization of the Hamiltonian is needed due to the energy independency of the wavefunctions which makes the LAPW approach much faster than the APW method. The accuracy of this particular method can be tuned by changing the muffin-tin radius (R_{MT}). Increasing the R_{MT} leads to an increase of region I (see Figure 2). The remaining smoother part of the wavefunction that has to be described by plane waves is getting smaller. Therefore less plane waves are needed, which leads to a reduction of the size of the matrices and evidently

will cost less computational time. R_{MT} should not become too large, because the spherical functions are not suited to properly describe the wavefunction far away from the nucleus. A compromise has to be made between the required accuracy and the available computational resources and can simply be applied by changing R_{MT} .

The Wien2k package [29] uses the FLAPW approach (Full potential Linear Augmented Plane Waves). Full potential means that all electrons are properly described and no shape approximation for the potential and charge density is used. This program was mainly used for exact electronic structure calculations.

2.3.4 Linearized Muffin-Tin Orbital (LMTO)

The LMTO method is also a linear method which is based on the APW approach. The main difference is, however, that the outer part of the wavefunction (region II) is not described by plane waves but by Hankel functions. Muffin-tin potentials or also an all-electron (full potential) approach can be used for the wavefunctions inside the muffin-tin spheres. In addition the LMTO method is often used in combination with the atomic sphere approximation (ASA). Within this approximation the muffin-tin spheres are blown up until they cover 100 % of the unit cell volume. Consequently, the interstitial region II completely vanishes and the spheres will overlap with each other. The amount of overlap of the spheres is decisive and can be reduced by the introduction of so-called empty spheres, i.e. additional spheres without atomic nuclei. The TB-LMTO-ASA package [30] combines the ASA with the LMTO method. Moreover, the tight binding (TB) approach is implemented into the TB-LMTO-ASA package and it originates from the assumption that the electrons are *tightly* bonded to their nuclei and therefore the LCAO ansatz (Linear Combination of Atomic Orbitals) can be applied. The crystal wavefunction is just a Bloch sum of the simplified Equation 9:

$$\psi(k) = \sum_n c_n \phi_{k_n} = \sum_n e^{ikr_n} \phi_{k_n} \quad (10)$$

The coefficients are determined by the Rayleigh-Ritz variational principle. The LCAO ansatz and therefore the similarity with the Hückel methods gives this

approach an intuitive interpretation of crystal bands since they are build from localized atomic orbitals. The accuracy, however, does not only depend on the basis set but also on the description of the Hamiltonian and overlap matrices. In our case (TB-LMTO-ASA) this is done within the framework of density-functional theory and thus without the use of any parameterization.

2.3.5 Bonding analysis: COHP

The crystal orbital Hamilton population (COHP) method [31] is used to analyze bonding interactions between atoms and is implemented in the TB-LMTO-ASA package. This technique can be compared with the crystal orbital overlap population (COOP) which is built on the Mulliken population analysis [32]. The latter one represents an arbitrary electron partitioning in terms of atoms and bonds. The COHP uses an energy resolved bonding descriptor which has already been successfully applied in plenty of different systems [33–35].

As a consequence of the LCAO ansatz (Tight-Binding in LMTO) the eigenvalue one-electron problem can be written as:

$$\sum_{LL'} (H_{LL'} - \epsilon_j S_{LL'}) c_{LL'j}^* c_{LL'j} = 0 \quad (11)$$

where $H_{LL'}$ and $S_{LL'}$ are abbreviations of

$$H_{LL'} = \langle \phi_L | \hat{H} | \phi_{L'} \rangle \quad S_{LL'} = \langle \phi_L | \phi_{L'} \rangle \quad (12)$$

The band energy is defined as the sum over all occupied one-electron eigenvalues (Equation 13, left). Moreover, it can be expressed as the energy integral of the distribution of the one-electron eigenvalues (Equation 13, right).

$$E^{\text{Band}} \equiv \sum_j f_j \epsilon_j \equiv \int^{\epsilon_F} d\epsilon \sum_j f_j \epsilon_j \delta(\epsilon_j - \epsilon) \quad (13)$$

Combining Equation 11 and 13 leads to:

$$\begin{aligned} \sum_j f_j \epsilon_j \delta(\epsilon_j - \epsilon) &= \sum_{LL'} H_{LL'} \sum_j f_j c_{LL'j}^* c_{LL'j} \delta(\epsilon_j - \epsilon) \\ &= \sum_{LL'} H_{LL'} \text{DOS}_{LL'}(\epsilon) \\ &= \sum_{LL'} \text{COHP}_{LL'}(\epsilon) \end{aligned} \quad (14)$$

The equation above indicates the close relation between the density-of-states (DOS) and the COHP, since the latter is constructed by weighting the DOS with the Hamilton matrix. The off-site COHP terms ($L \neq L'$) indicate the interactions between the atoms. If there are bonding contributions, the system undergoes a lowering of its energy, indicated by negative off-diagonal COHPs. On the other side, if a structure is destabilized by antibonding contributions, there will be positive off-diagonal COHPs. For the purpose of comparison with the well established COOP, the negative COHP is plotted. Therefore the positive/negative region indicates the bonding/antibonding interactions.

3. Binary Oxides and Nitrides of the First-Row Transition Metals

In this section it will be investigated if the experimental properties of the $3d$ transition-metal oxides and nitrides (MN and MO, M = Sc, Ti, V, Cr, Mn, Fe, Co, Ni) can be properly reproduced by density-functional theory. First this is done as a test to explore the limitations of DFT and, second, the results of these investigations will be used to prove that the oxynitrides of the $3d$ transition metals are more than just combinations of the archetypical binary compounds. The growing interest for these two binary classes has led to an enlarged database of properties. The structural, electronic and magnetic properties of the $3d$ transition-metal oxides and nitrides are listed in Table 1. The data were taken from the Inorganic Crystal Structure Database (ICSD) and literature cited within [6].

	Structure		Electrical Prop.		Magnetic Prop.	
	Oxide	Nitride	Oxide	Nitride	Oxide	Nitride
Sc	NaCl	NaCl	metal	metal	P	-
Ti	NaCl	NaCl	metal	metal	P	P
V	NaCl	NaCl	metal	metal	P	P
Cr	NaCl	NaCl ^d	-	semicond.	-	AFM
Mn	NaCl	NaCl ^d	insulator	metal	AFM	AFM
Fe	NaCl	ZnS	insulator	metal	AFM	P
Co	NaCl	ZnS	insulator	metal	AFM	P
Ni	NaCl	-	insulator	-	AFM	-

Table 1: Experimental properties of the 1:1 binary $3d$ transition-metal oxides and nitrides. P = paramagnetic; AFM = antiferromagnetic. (^d indicates a distorted structure)

All monoxides crystallize in the rocksalt structure. The first three (ScO, TiO, and VO) are reported to be paramagnetic and metallic, and the remaining ones are insulating antiferromagnetic compounds. Apparently, at CrO, there is a change in the electrical and magnetic properties. It is therefore too bad that CrO is not well investigated and that only its structure is known.

The nitrides are somewhat different. Only the nitrides of scandium, titanium, and vanadium adapt the cubic rocksalt structure. Chromium and manganese nitride crystallize in a distorted form of rocksalt, whereas CrN is orthorhombic and MnN is tetragonally distorted. A structural change, from rocksalt to zinc blende, is observed when moving on to iron and cobalt nitride. Nickel nitride has not been synthesized yet, although theoretical calculations predict its structure as being zinc blende [34]. A more complete overview of the crystallographic data of the transition-metal oxides and nitrides is listed in Appendix B.

3.1 First-Row Transition-Metal Oxides

As mentioned before, all the $3d$ transition-metal oxides adapt the rocksalt structure. Among them, ScO [36, 37], TiO [38], and VO [36, 39] are paramagnetic metallic conductors, and MnO [40, 41], FeO [42], CoO [43] and NiO [38] are antiferromagnetic insulators. CrO has been synthesized but not well investigated yet [36]. In this section it will be investigated whether the calculated properties of the oxides match reality. One may assume that a correct description of the experimental properties is also indicative of the correct total energies of the oxides. The latter are needed for the calculation of the relative stability of the $3d$ transition-metal oxynitrides (Section 4.2). Therefore the energies of the oxides in both the rocksalt and zinc blende structures for a nonmagnetic, a ferromagnetic and an antiferromagnetic arrangement are compared and the most stable configuration is determined. This calculated stable configuration is compared with the experimental properties. The antiferromagnetic states, referred to in Table 2, are the [111] arrangements, which can be characterized as a sequence of ferromagnetically sheets aligned along [111] which alternate in sign. All calculated energies refer to the energy of the experimental ground state. Calculated

energies which are even lower than the energies of the experimental phases are symbolized in bold.

	NaCl			ZnS		
	NM	FM	AFM	NM	FM	AFM
Sc	0	-	-	0.346	-	-
Ti	0	-	-	0.317	-	-
V	0	-0.094	-0.511	-0.007	-0.332	-0.358
Cr	1.361	0.297	0	0.929	0.419	0.142
Mn	2.096	0.156	0	1.332	1.303	-0.281
Fe	1.411	0.023	0	0.670	0.640	0.630
Co	0.656	0.215	0	0.259	-0.063	-0.202
Ni	0.334	0.260	0	0.251	0.104	0.183

Table 2: Calculated (GGA) total energies (eV/f.u.) of the $3d$ transition-metal oxides with different spin-orientations relative to the experimental phases. NM = nonmagnetic; FM = ferromagnetic; AFM = antiferromagnetic

First of all the structural properties will be examined and hereby the relative energies of the oxides in the rocksalt and the zinc blende structure are compared. The results from Table 2 show that the calculations are in fair agreement with the experimental results in terms of structure. The rocksalt structure is preferred by all oxides except MnO and CoO. The relative energies of Table 2 show an incorrect preference of these oxides for the zinc blende structure of 0.281 and 0.202 eV, respectively. An explanation for this mismatch will be given later on.

Moreover the oxides are calculated in three different magnetic arrangements. The calculations show that ScO and TiO are nonmagnetic, which is in good agreement with the experimental results. All other oxides prefer the experimentally found [111] antiferromagnetic arrangement independent of the structure type. MnO and CoO have the lowest energy in the erroneous zinc blende structure, but they also favor to be antiferromagnetic. Surprising is the fact that VO also seems to prefer this antiferromagnetic arrangement, although it should be

paramagnetic with respect to experimental results. Until now, no experimental proof has been given for this antiferromagnetic arrangement, but these results are confirmed by previous calculations performed by Mackrodt *et al.* [44]. The unknown phase of CrO is predicted to also be antiferromagnetic. At this point one may say that DFT surprisingly handles the transition-metal oxides quite well, taking only the structural and magnetic properties into account.

The next step is to determine whether the electrical properties of the transition-metal oxides can also be described by DFT. Therefore the band gaps of these oxides will be calculated and compared with the experimental results. The theoretical investigations show that ScO, TiO, and VO are metallic conductors, which is again in good agreement with the experimental results from Table 1. The highly correlated oxides MnO, FeO, CoO, and NiO are insulators and pose a real challenge to density-functional theory. For this reason a comparison between the experimental and calculated band gaps of these compounds is given in Table 3.

	Band gap exp.	Band gap calc.
MnO	3.6–3.8	1.5
FeO	> 3.5	metal
CoO	> 3.0	metal
NiO	3.9–4.3	0.2

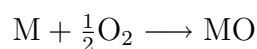
Table 3: Experimental and calculated (GGA) band gaps (eV) for MnO, FeO, CoO and NiO in the rocksalt structure.

The range of experimental band gaps may be caused by the broad compositional phase width of the 3d transition-metal oxides, e.g., Mn_xO with $0.848 \leq x \leq 1.000$. The calculations say that FeO and CoO should be metallic conductors, NiO should be a small bandgap semiconductor and MnO should be a semiconductor with a bandgap of 1.5 eV. Thus, the bandgaps are all incorrectly calculated. Despite the fact that the structural and magnetic properties of FeO and NiO are correct, the calculated electronic structures for these oxides are not. The only conclusion which can be made at this point is that DFT fails

for MnO, FeO, CoO, and NiO. This, however, is a well-known problem [45–49]. One possible solution is given by the augmentation of DFT with an empirical parameter (Hubbard U) for interelectronic correlation [50]. The choice of the magnitude of U is somewhat arbitrary and therefore a matter of debate.

The conclusion so far is that DFT describes the structural, electrical, and magnetic properties of ScO, TiO, VO, and CrO quite well. The highly correlated oxides (MnO, FeO, CoO, and NiO), however, appear as a challenge for DFT. The properties of these oxides cannot be reproduced by DFT calculations. It will now be investigated whether the total energies of the transition-metal oxides are correct or not. As mentioned before, the correct total energies of these oxides are needed to determine the relative stability of the $3d$ transition-metal oxynitrides in comparison to the transition-metal nitrides and oxides. Instead of adjusting the total energies with a DFT correction like the Hubbard U , the knowledge of experimental calorimetric results can also be taken into account. Calorimetric measurements show that the rocksalt structure of CoO is 37 kJ/mol more stable than the zinc blende phase. Since CoO is the only $3d$ transition-metal oxide which has been synthesized in the zinc blende phase, however, this approach can only be applied to cobalt oxide [51, 52].

A more general attempt is to compare the calculated and experimental formation enthalpies. The formation enthalpy is calculated by subtracting the sum of total energies of the transition metal and the oxygen from the total energy of transition-metal oxide.



The calculated total energy can be regarded as an enthalpy ($H = E + pV$), because the pressure is close to zero such that the “ pV ” term vanishes. The calculated and experimental formation enthalpies are listed in Table 4. They all refer to the rocksalt phase of the transition-metal oxides. No experimental data are available for ScO and CrO.

All formation enthalpies are calculated too small in comparison with the experimental values. These difference can, to some degree, be explained by the temperature dependence of the formation enthalpy, since the calculations were

	Calc. ΔH_f^0	Exp. ΔH_f^0	$\Delta\Delta H_f^0$
ScO	-566.4	-	-
TiO	-472.2	-542.7	68.5
VO	-351.7	-431.8	80.1
CrO	-301.4	-	-
MnO	-313.3	-384.9	71.6
FeO	-204.9	-272.0	67.1
CoO	-182.8	-237.7	54.9
NiO	-211.2	-239.7	28.5

Table 4: Calculated and experimental formation enthalpies (kJ/mol) of the $3d$ transition-metal oxides. $\Delta\Delta H_f^0$ is the difference between the experimental and calculated ΔH_f^0 .

all performed at absolute zero. The experimental results, however, refer to room temperature (298 K). This temperature dependence, from 0 to 298 K, of the oxide's formation enthalpy has to be considered too. This is about 18.5 kJ/mol [53]. Also the melting enthalpy of oxygen (0.22 kJ/mol) and the vaporization enthalpy (3.41 kJ/mol) are neglected [53]. Thus, minor differences of about 22 kJ/mol between the calculated and experimental formation enthalpies can be explained by including the just mentioned enthalpies. But, as can be seen, from Table 4 the differences between experiment and theory are much larger. They are all in the range of about 55–80 kJ/mol (except for NiO). It seems that DFT has a systematic error either in describing the transition-metal oxides or in describing the single elements (transition metals and oxygen). The differences between the experimental and calculated formation enthalpies of the transition-metal oxides are plotted in Figure 3.

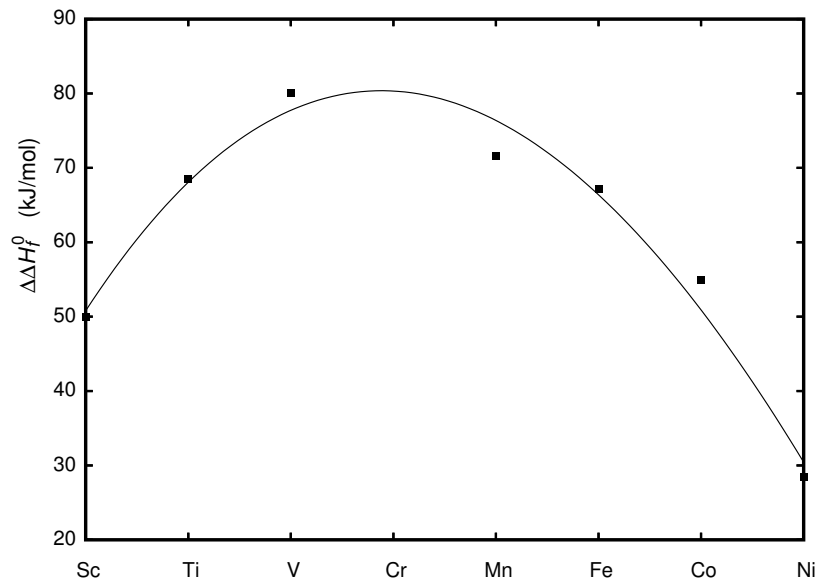


Figure 3: Differences between the theoretical and experimental formation enthalpy, $\Delta\Delta H_f^0$ (kJ/mol) for the 3d transition-metal oxides.

The figure shows that the underestimation of interelectronic correlation is largest in the middle of the 3d row and falls off for the early/late 3d metals. The used DFT method can only give a qualitative description of the 3d transition-metal oxides, even though the properties of some oxides (ScO, TiO, VO and CrO) are correctly calculated. Therefore the experimental formation enthalpies will be used for further investigations.

3.2 First-Row Transition-Metal Nitrides

The first aim is to calculate the electronic structures of the nitrides in the two mentioned structure types and compare the calculated results with the experimental ones. This will be done, again as a kind of test for the used theoretical methods and explore the possibility to derive and predict properties of the oxynitrides directly from the properties of the binary compounds. Therefore, the total energy of the nitrides (Table 5) is calculated and compared with the experimental results. The calculations were performed with different spin-orientations denoted as nonmagnetic, ferromagnetic and antiferromagnetic, where the lat-

ter one is an orthorhombic antiferromagnetic (110) arrangement for CrN and a tetragonally distorted (100) arrangement for MnN.

	NaCl			ZnS		
	NM	FM	AFM	NM	FM	AFM
Sc	0	-	-	0.653	-	-
Ti	0	-	-	0.652	-	-
V	0	-	-	0.306	0.288	-
Cr	0.597	0.232	0 ^d	0.388	0.059	0.092
Mn	0.821	0.096	0 ^d	0.109	0.103	0.109
Fe	0.979	0.665	-	0	-	-
Co	0.763	-	-	0	-	-
Ni	0.390	-	-	0	-	-

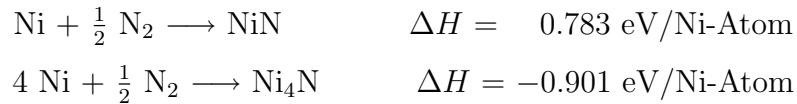
Table 5: Calculated total energies (eV/f.u.) of the 3d transition-metal nitrides with different spin-orientations relative to the experimental phases. NM = nonmagnetic; FM = ferromagnetic; AFM = antiferromagnetic. (^d distorted structure)

The results for ScN, TiN and VN are unambiguous. The rocksalt structure is preferred over the zinc blende structure which is in accordance with the experimental results [39, 54–56]. There is, as expected, no preference for a ferromagnetic ground state. CrN and MnN are a little peculiar in comparison with the rest since they do not have a cubic ground state. At the Néel temperature ($T_N = 273\text{--}286\text{ K}$), CrN undergoes both a structural and a magnetic transition to an antiferromagnetic (AFM) orthorhombic $Pnma$ phase [57]. In the case of CrN, the driving force for this distortion seems to be magnetic stress, as proposed by Filippetti *et al.* [58]. The results in Table 5 confirm these experimental findings. The calculations of MnN are also in very good agreement with the experiment and favor the antiferromagnetic distorted rocksalt type for MnN [59–61].

A structural change from rocksalt to zinc blende happens at the later transition-metal nitrides (Fe and Co) [62, 63]. These findings clearly show a thermodynamical preference of the nitrides of iron, cobalt and nickel for the nonmagnetic zinc blende phase, since the energy differences between the zinc blende and

rocksalt structure of FeN and CoN are about 64 kJ/mol and 74 kJ/mol respectively. Therefore, it seems very unlikely that FeN and CoN can be obtained in the rocksalt structure. Nonetheless rocksalt type FeN and CoN have been synthesized with sophisticated experimental efforts. Cubic rocksalt iron nitride is denoted as γ''' -FeN [64]. The existence of rocksalt CoN may be questioned since the experimentally found lattice parameter of 4.27 Å for the rocksalt phase [65] is very close to the one found for zinc blende CoN (4.28 Å [63], 4.297 Å [66]).

The calculated energy differences between the two structure types for CrN and MnN are considerably smaller ($\Delta E \approx 10$ kJ/mol). It is therefore surprising that they only exist in the rocksalt structure and not in the zinc blende structure. Moreover NiN does not exist at all. The results from Table 5, however, indicate a clear preference for the zinc blende structure. Why could NiN not be synthesized yet? The answer to this question is found in the following equations:



NiN is unstable in comparison to the elements Ni and $\frac{1}{2}\text{N}_2$. On the contrary, Ni_4N is more stable than the elements, which leads to the conclusion that synthesis of NiN, under thermodynamically controlled conditions, always leads to Ni_4N .

The calculations coincide very well with the experimental electronic and structural properties of the binary $3d$ nitrides and the lattice parameters and volumes should therefore also be reproducible. Generally the GGA (generalized gradient approximation) calculations result in lattice parameters which are larger than the experimental ones [16]. Using the LDA (local-density approximation), however, the lattice parameters are too small. Thus, the lattice parameter of a precisely stoichiometric nitride (1:1) should be somewhere in the middle between the two used approximations (GGA and LDA). If this is not the case, it can be concluded that the experimentally synthesized transition-metal nitride is not precisely 1:1 stoichiometric. An experimental lattice parameter (or volume) which is larger/smaller than the calculated using GGA/LDA, indicates additional occupied sites/empty sites within one sublattice. The experimental

volumes (filled boxes) are shown in Figure 4 as well as the calculated volumes, using the LDA- (solid line) and GGA-functional (dashed line) for the most stable ground state. The line between the data entries has no physical meaning and is only a guide to the eye.

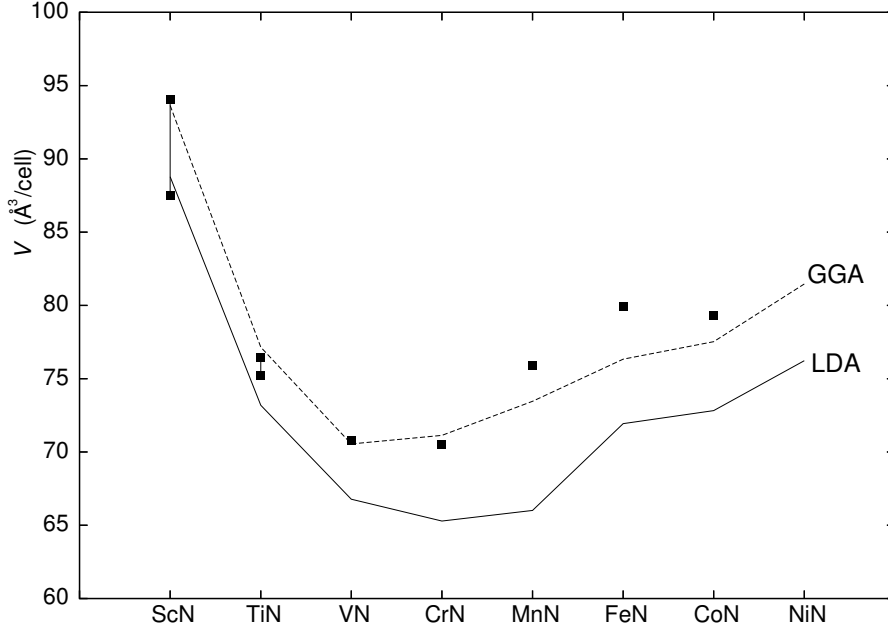


Figure 4: Experimental and calculated (GGA and LDA) volumes for the $3d$ transition-metal nitrides. LDA = solid line, GGA = dashed line and experimental = filled boxes.

The results presented in Figure 4 show a broad range of experimental volumes for ScN and TiN which indicates the broad compositional range. The experimental volumes of VN and CrN are between the calculated LDA and GGA volumes. This indicates that for these compounds the transition metal-nitrogen ratio is very close to 1. On the other hand the experimental volumes of MnN and especially FeN and CoN are significantly larger than the calculated GGA volumes. This indicates that, iron nitride for example, in the literature always reported as $\text{FeN}_{0.91}$, is not the correct formula. This formula presumes empty sites within the nitrogen sublattice which should lead to a smaller volume. Therefore iron nitride should better be written as $\text{Fe}_{1.1}\text{N}$. Notice that the Fe:N ratio in both formulas is the same. The latter formula only implies that additional sites in the iron sublattice are occupied and explains why the experimental volume is

larger than the calculated (GGA).

The geometric and electronic structures of the first row transition-metal nitrides are correctly calculated. The early nitrides (ScN–MnN) crystallize in the rocksalt structure. The cubic cell is tetragonal or distorted orthorhombic for MnN and CrN respectively. The latter ones have an antiferromagnetic spin arrangement. All the other $3d$ transition-metal nitrides are para- or Pauli-paramagnets. FeN and CoN adopt the zinc blende structure, which is also predicted for NiN, but the latter has unfortunately not been synthesized yet.

If the oxynitrides of the $3d$ transition metals are simple combinations of the corresponding nitrides and oxides, a first crude prediction of their properties can be made at this point. Combining the results of the first row metal oxides and nitrides, $\text{ScO}_x\text{N}_{1-x}$, $\text{TiO}_x\text{N}_{1-x}$ and $\text{VO}_x\text{N}_{1-x}$ should adopt the rocksalt structure. $\text{CrO}_x\text{N}_{1-x}$ and $\text{MnO}_x\text{N}_{1-x}$ will probably also favor the rocksalt structure, which could be distorted. The structural properties of the later $3d$ transition-metal oxynitrides are much more difficult to predict, since the oxides prefer the rocksalt structure but the nitrides change into the zinc blende structure. A reliable prediction of the electronic and magnetic structure of the oxynitrides seems to be even more difficult. The only reasonable solution is to calculate the oxynitrides as well. The results are presented in Section 4.

4. Oxynitrides of the 3d Transition Metals

Within the recent years there is a growing interest in oxynitride materials, both in the fundamental and applied fields. The driving force for the ongoing research clearly originates from the believe that oxynitrides, either containing main-group- or transition-metals, can be chemically tuned such as to combine the best mechanical and also electronic properties of both binary material classes (oxides and nitrides). In spite of the promising goal, oxynitride chemistry is difficult, illustrated by the fact that only a few transition-metal oxynitrides have been synthesized and characterized yet, for example TaON [67, 68], Zr_2ON_2 [69] and CoO_xN_{1-x} [70]. Even though there are several experimental publications on these materials and the majority of these contributions emphasizes both synthesis and possible chemical applications, the physical properties of these compounds play a minor role. It is quite surprising that the structural properties of only a few of these compounds, namely CoO_xN_{1-x} [70], VO_xN_{1-x} [71] and CrO_xN_{1-x} [72, 73], are known to some degree. VO_xN_{1-x} and CrO_xN_{1-x} are reported to exist in the rocksalt structure and CoO_xN_{1-x} is experimentally suggested and theoretically supported [74] to adopt the zinc blende structure. Whether polymorphism is important for the 3d oxynitrides (MO_xN_{1-x}) is another challenging question. Titanium- and iron oxynitrides have also been synthesized but their exact structures have not been determined yet [75, 76]. The oxynitrides of scandium, manganese and nickel still wait for their discoveries.

4.1 3d Transition-Metal Oxynitrides; Structure and Magnetism

The daltonide binary oxides and nitrides of the 3d row transition metals crystallize either in the rocksalt or in the zinc blende structure. Therefore, these two structure types were considered for the investigation of the 3d transition-metal oxynitrides ($\text{MO}_x\text{N}_{1-x}$; $M = \text{Sc-Ni}$), too. The main difference between the archetypical oxides and nitrides and the oxynitrides is that the latter group is distinguished by a variable anion order and composition. These features complicate the theoretical goal enormously. For economical reasons, the calculations presented here were performed on $x = 0.5$ systems ($\text{MO}_{0.5}\text{N}_{0.5}$) and should be considered model-like approaches needed to scan the systems in the very first place. In addition, non-spin-polarized (nonmagnetic) calculations were performed at the beginning to ease understanding (see below).

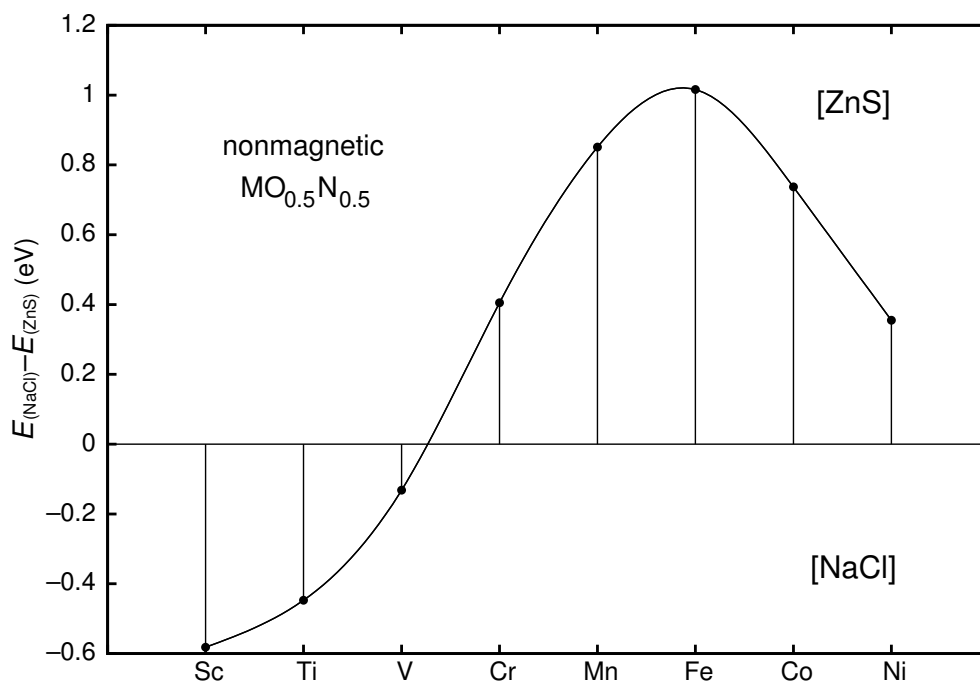


Figure 5: Energy difference between the 3d transition-metal oxynitrides in the rocksalt and the zinc blende type, for the nonmagnetic case.

Figure 5 presents a plot of the energy differences between the rocksalt and zinc blende type structures for these oxynitrides. The calculations are based on the plane-wave/pseudopotential approach, and the line between the data entries has no physical meaning but is only a guide to the eye.

In the positive energy region the zinc blende type is preferred, whereas in the negative region the rocksalt type is favored. The results of these calculations turn out as qualitatively correct because they predict that the earlier oxynitrides will adopt the rocksalt type whereas the later ones will crystallize in the zinc blende type; in fact, $\text{VO}_{0.5}\text{N}_{0.5}$ adopts [NaCl] whereas $\text{CoO}_{0.5}\text{N}_{0.5}$ adopts [ZnS]. The quantitative prediction of the crossover is incorrect, though, because $\text{CrO}_{0.5}\text{N}_{0.5}$ is falsely predicted to adopt also [ZnS] but this problem is due to the omitted inclusion of magnetism. The same trend ([NaCl] \rightarrow [ZnS]) occurs for the transition-metal nitrides [34] and has been explained already. Let us qualitatively understand why the zinc blende structure is preferred to the rocksalt structure for higher electron counts and analyze the electronic structures of both polymorphs in more detail. For this purpose the chemical bonding situations were analyzed using the Crystal Orbital Hamilton Population (COHP) technique, and $\text{CrO}_{0.5}\text{N}_{0.5}$ was taken as an example.

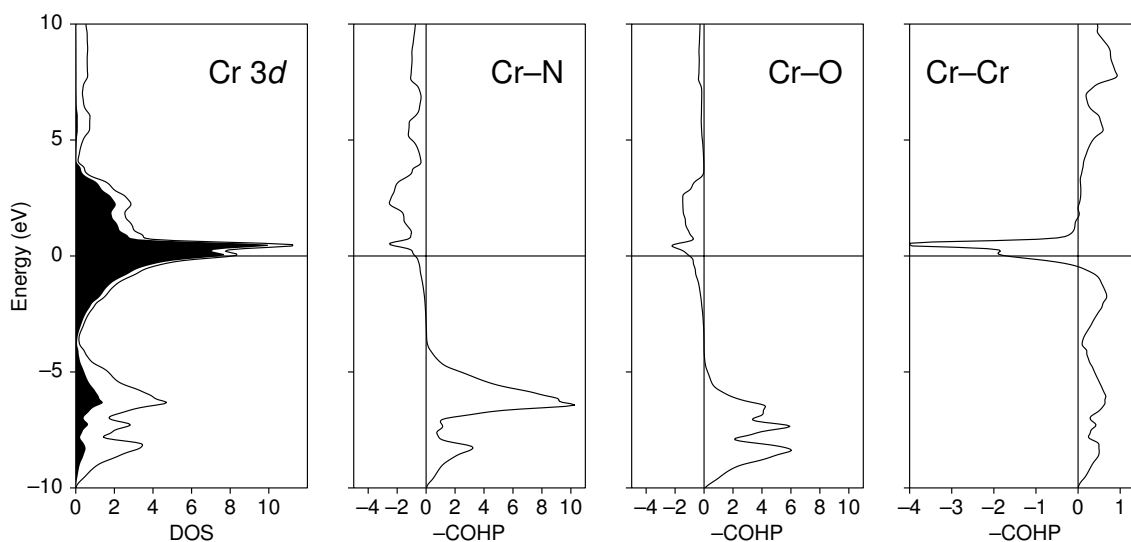


Figure 6: Density-of-states (DOS) with local 3d projections, and crystal orbital Hamilton populations (COHP) for the Cr–N, Cr–O and Cr–Cr interactions in the lowest-energy rocksalt type structure of $\text{CrO}_{0.5}\text{N}_{0.5}$.

The density-of-states (DOS) at the Fermi level is rather high for rocksalt-like $\text{CrO}_{0.5}\text{N}_{0.5}$ (Figure 6), mainly caused by Cr 3d orbital contributions. The COHP diagrams for the metal-nonmetal interactions, Cr–N and Cr–O, show strong bonding contributions between *ca.* -8 and -4 eV which actually stabilize the structure. On the other side, there are also strong, unfavorable Cr–Cr *antibonding* interactions (spikes to the left) at the Fermi level, a consequence of the adopted structure type.

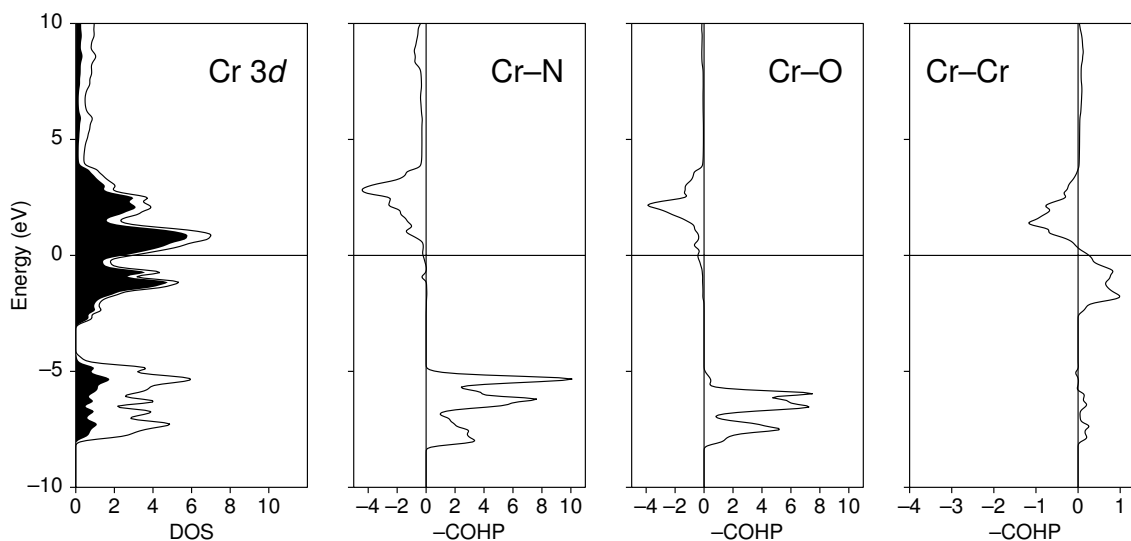


Figure 7: Density-of-states (DOS) with local 3d projections, and crystal orbital Hamilton populations (COHP) for the Cr–N, Cr–O and Cr–Cr interactions in the lowest-energy zinc blende type structure of $\text{CrO}_{0.5}\text{N}_{0.5}$.

The DOS diagram of $\text{CrO}_{0.5}\text{N}_{0.5}$ in the zinc blende structure (Figure 7) also shows a significant density-of-states at the Fermi level, indicating the metallic nature of this compound, also mainly made up from Cr 3d contributions. The low-lying peaks around -7.5 and -5 eV are caused by nitrogen/oxygen 2p orbitals. The latter ones are separated by an internal 1.9 eV-wide gap from the “cationic” Cr 3d states at the Fermi level. There are very strong Cr–N and Cr–O bonding interactions at *ca.* -6 eV, just like for the preceding [NaCl] structure. The integrated chromium–nitrogen and chromium–oxygen COHPs are quite similar for the rocksalt (Cr–N: -3.413 eV/bond, Cr–O: -2.145 eV/bond) and for the zinc blende structure (Cr–N: -3.635 eV/bond, Cr–O: -2.283 eV/bond)

but indicate that the bonding is more covalent in the [ZnS] structure type. The most prominent difference, however, is found in the Cr–Cr COHP curve because the formerly antibonding Cr–Cr interactions at the Fermi level have now been turned into bonding interactions. This finding is a trivial consequence of the zinc blende type structure in which the Cr–Cr distances are wider (3.18 Å) than in the rocksalt structure (3.00 Å) such that the “excess” electrons residing on Cr do not destabilize the zinc blende type as much as the rocksalt type.

A closer look at the Cr–Cr COHP curve in an energy window around the Fermi level (from -3 eV to 4 eV) allows the direct comparison, and a rigid band model can be adopted since the COHP curves of $\text{MO}_{0.5}\text{N}_{0.5}$ ($M = \text{Sc-Ni}$) are quite similar to those of $\text{CrO}_{0.5}\text{N}_{0.5}$; recall that this proposal is a *qualitatively* correct but simplified explanation. Thus, the two COHPs of the Cr–Cr interaction are shown in Figure 8 where the arrows indicate the relative position of the Fermi level for the other transition-metal oxynitrides. As expected, the Fermi level ϵ_F is shifted up when moving from scandium to nickel.

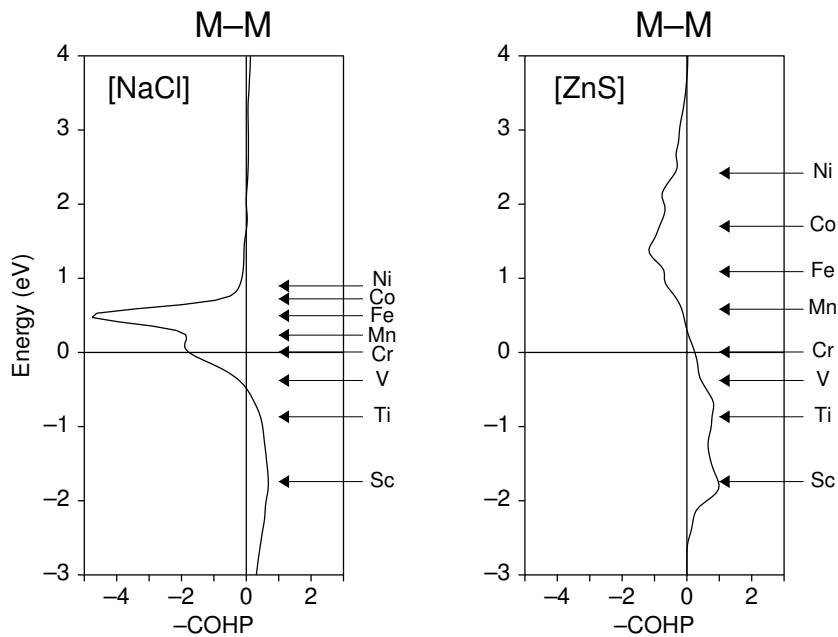


Figure 8: Crystal Orbital Hamilton Populations (COHP) for the Cr–Cr interactions of $\text{CrO}_{0.5}\text{N}_{0.5}$ in the rocksalt type (left) and the zinc blende type (right) structure. The arrows denote the Fermi levels in the other isostructural compounds.

As seen in the COHP of the rocksalt structure in Figure 8, the Fermi levels for Sc and Ti are situated in the metal–metal bonding region, indicative of the stability of the nonmagnetic rocksalt structure type for $\text{MO}_{0.5}\text{N}_{0.5}$. Moving up to V, the Fermi level switches from metal–metal bonding to slightly antibonding already. Putting even more electrons into the system, that is, in the proximity of $\text{CrO}_{0.5}\text{N}_{0.5}$, the Fermi level is clearly situated in the antibonding region which destabilizes the rocksalt structure. Nonetheless the Fermi level for the zinc blende structure is still situated in the bonding region (see right curve in Figure 8). Therefore, the change from the rocksalt to the zinc blende structure becomes advantageous for higher electron concentrations.

The complexity of this theoretical treatment will now be increased to allow more quantitative conclusions. Besides a structural change, the stabilization of a given phase can be achieved by spin polarization leading to different spin-occupations and a magnetization of the compound. For this reason, the next step is to allow the systems to become magnetic in the theoretical description. Thus, all preceding plane-wave/pseudopotential calculations for $\text{MO}_{0.5}\text{N}_{0.5}$ adopting the ZnS/NaCl types were repeated, but now including spin polarization; the magnetic moments, if present, were allowed to couple either ferromagnetically or antiferromagnetically.

Keeping in mind the COHPs in Figure 8, one would expect no structural or electronic distortion for the oxynitrides of scandium and titanium because of ϵ_F being localized in the bonding region; in particular, spontaneous spin polarization should not result from M–M states!

On the contrary the rocksalt structure of chromium- and manganese oxynitride would be susceptible to spin polarization because their Fermi levels are situated in the *antibonding* area of the M–M COHP. This prediction would also hold for the later first row transition-metal (Fe, Co and Ni) oxynitrides but, since they adopt the zinc blende structure where these antibonding interactions are significantly reduced, the susceptibility to spin polarization should be much smaller. The numerical results of all the calculations are shown in Figure 9, which has the same layout as Figure 5. In addition, the most stable spin arrangement for each structure type is used in this "magnetic" diagram.

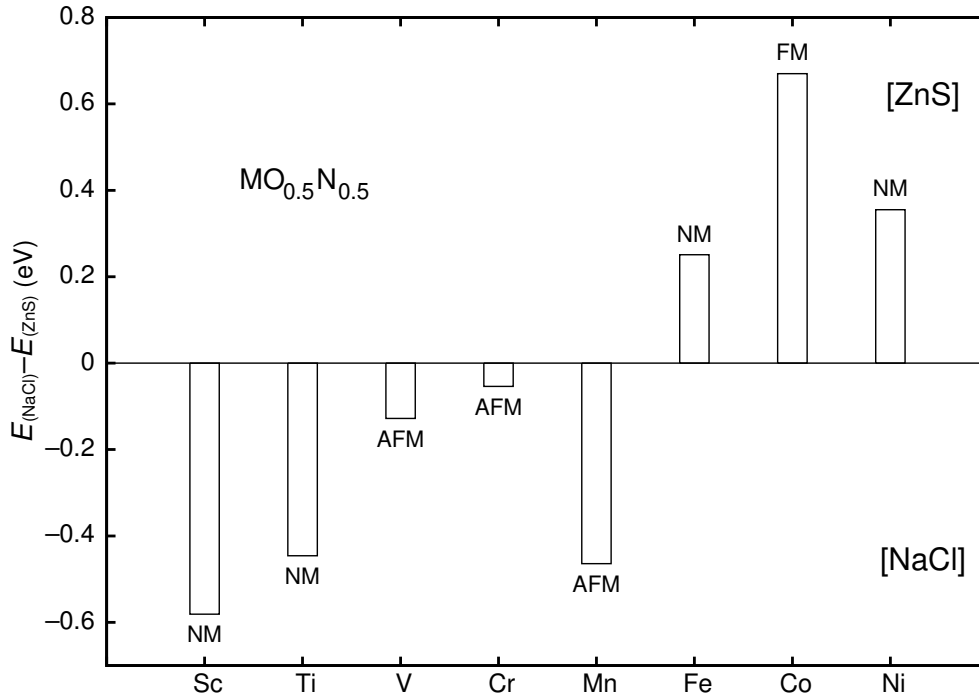


Figure 9: Energy difference between the 3d transition-metal oxynitrides in the rocksalt and the zinc blende type for the most stable spin arrangement. The type of spin arrangement is denoted in the picture as 'NM' for nonmagnetic, 'FM' for ferromagnetic and 'AFM' for the antiferromagnetic ordering.

As far as density-functional theory can be trusted, its predictions fulfill these simple expectations (see above) by yielding that $\text{ScO}_{0.5}\text{N}_{0.5}$ and $\text{TiO}_{0.5}\text{N}_{0.5}$ should crystallize in the rocksalt structure and should also be nonmagnetic. Phases with critical M–M antibonding electron counts ($\text{VO}_{0.5}\text{N}_{0.5}$, $\text{CrO}_{0.5}\text{N}_{0.5}$, $\text{MnO}_{0.5}\text{N}_{0.5}$) may still stick to the [NaCl] structure type but lower their energies by building up local magnetic moments; the latter are antiferromagnetically coupled along [100]. A structural change is finally seen for the later 3d oxynitrides because $\text{FeO}_{0.5}\text{N}_{0.5}$, $\text{CoO}_{0.5}\text{N}_{0.5}$ and $\text{NiO}_{0.5}\text{N}_{0.5}$ prefer the zinc blende type. In a first approximation $\text{FeO}_{0.5}\text{N}_{0.5}$ and $\text{NiO}_{0.5}\text{N}_{0.5}$ are nonmagnetic and $\text{CoO}_{0.5}\text{N}_{0.5}$ appears to be ferromagnetic.

The accurate theoretical determination of the relative stabilities of structure and magnetism of the later 3d oxynitrides is problematic because of two rea-

sons. First, the systems are likely to show strong effects of electronic correlation such that density-functional theory may reach its limits. Second, anionic order/disorder competes with spin polarization: in Section 4.3 it will be shown that a largely disordered $\text{CoO}_{0.5}\text{N}_{0.5}$ loses its local magnetic moments [74], and for the here investigated and *less* disordered $\text{CoO}_{0.5}\text{N}_{0.5}$ the energy difference between the magnetic and nonmagnetic state (≈ 0.017 eV/f.u.) is less than a third of the energy gain upon complete O/N disordering. An exception is made with $\text{MnO}_{0.5}\text{N}_{0.5}$ because of the very large exchange splitting of the Mn atom. This oxynitride clearly spin-polarizes and the antiferromagnetic structure is about 1.34 eV/f.u. more stable than the nonmagnetic structure. This implies that $\text{MnO}_{0.5}\text{N}_{0.5}$ has a specific magnetic spin arrangement, although a random anion order is probably preferred. The search for a magnetic 3d oxynitride should therefore be mainly focused on the synthesis of $\text{MnO}_{0.5}\text{N}_{0.5}$.

4.2 Thermodynamic Stability

In this section a closer look at the relative thermodynamic stability of the 3d transition-metal oxynitrides will be taken. The energy of the most stable oxynitride polymorph is compared with the energies of the corresponding binary oxides and nitrides. The formation energy, ΔE_f , of the ternary phase $\text{MO}_{0.5}\text{N}_{0.5}$ starting with the binary phases of MN and MO is calculated according to

$$\Delta E_f = E_{\text{MO}_{0.5}\text{N}_{0.5}} - \frac{E_{\text{MN}} + E_{\text{MO}}}{2}, \quad (1)$$

thereby emphasizing the importance of the correct energetic characterization of the two binary boundary phases, MN and MO. In a good approximation, the formation energy ΔE_f may be interpreted as an enthalpy (See Section 3.1). Since all the internal energies are negative, a negative value of ΔE attests a stabilization of the oxynitride in comparison to the oxide and nitride. Further, one must consider that density-functional theory fails for the highly correlated systems, as seen before in Section 3. Therefore, it is better to rely on experimental data. The experimental formation enthalpies (listed in Table 4) of the transition-metal oxides are used in Equation 1. The nitrides are properly calcu-

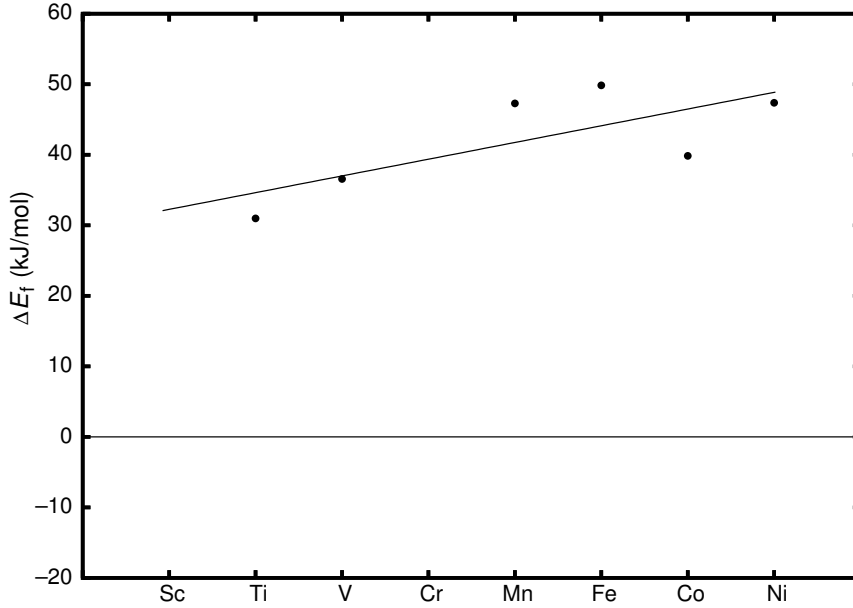


Figure 10: Formation energy of the $3d$ transition-metal oxynitrides relative to the binary oxides and nitrides.

lated and it can be assumed that the oxynitrides are also well described by DFT, because the later transition-metal oxynitrides (Fe, Co and Ni) adopt, in contrary to the oxides, the zinc blende structure. The relative energy differences between the oxynitrides and the binary phases are calculated according to Equation 1 and plotted in Figure 10.

The filled circles are the calculated values of the formation energy including the experimental formation enthalpies of the $3d$ transition-metal oxides. For ScO and CrO no experimental values are available. The line is fitted through these points to roughly indicate the relative stability of the oxynitrides and is only a guide to the eye. It seems that all $3d$ transition-metal oxynitrides are metastable with respect to the binary phases. This fact presumably explains why many of these oxynitrides have not been synthesized yet. It must be said that the calculations were performed using a simple cubic cell, from which only *one* ordered anion arrangement was taken into account. As mentioned before, a statistical anion distribution is probably favored and leads to a stabilization of the oxynitride. This, however, requires a very expensive and time-consuming supercell approach. An additional way of including a statistical anion order is

the consideration of the configurational entropy, which has already been applied to related systems, $\text{Si}_2\text{N}_2\text{O}$ [77] and Zr_2ON_2 [78], and is calculated according to:

$$S_{\text{mix}} = R \sum_i x_i \ln x_i \quad (2)$$

where x_i is the fraction of the corresponding atom (i) and R is the ideal gas constant ($8.314 \text{ J mol}^{-1} \text{ K}^{-1}$). The configurational entropy is based on the positional interchange of atoms, in this case the oxygen and nitrogen atoms. The value obtained from the equation above is $-5.763 \text{ J mol}^{-1} \text{ K}^{-1}$ which gives approximately 1.7 kJ/mol at room temperature. In comparison with the energy differences (ΔE) from Figure 10, the stabilization caused by the mixing entropy is very small. These results again confirm the experimental difficulties of the synthesis of 3d transition-metal oxynitrides. It seems that $\text{ScO}_{0.5}\text{N}_{0.5}$ should be thermodynamically less unstable and “simplest” to synthesize.

4.3 Supercell Stoichiometry

The enthalpic stability investigations from the last section will now be extended towards questions of phase width, magnetism and anionic order of the oxynitride compounds. To allow for a multitude of different compositions, a $2 \times 2 \times 2$ supercell is created, containing a total of 64 atoms of which 32 were transition metals and 32 either N or O as presented in Figure 11.

First of all, the anion order of the oxynitrides is investigated and therefore different anion arrangements within one specific stoichiometry; $\text{MO}_{0.5}\text{N}_{0.5} \equiv \text{M}_{32}\text{O}_{16}\text{N}_{16}$, are taken into account. The anion arrangements can be divided into one ordered phase and several randomly distributed anions. These several anion compositions are only calculated for the most stable structure type of the corresponding oxynitride. Since the supercell calculations are very time-consuming and expensive, they were only performed for the oxynitrides of scandium and cobalt. The results for the most stable random configuration are shown in Table 6.

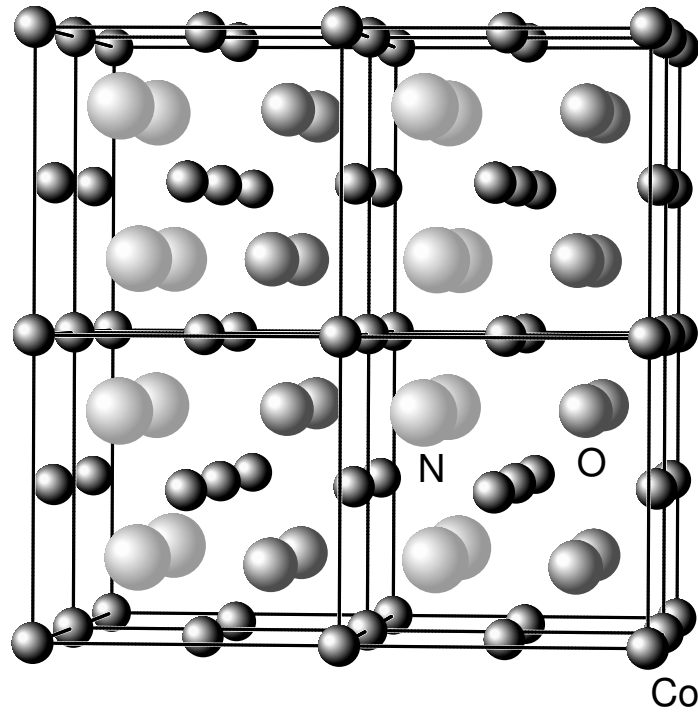


Figure 11: Supercell containing $2 \times 2 \times 2$ conventional cubic cells of the zinc blende structure of $\text{CoO}_{0.5}\text{N}_{0.5}$.

In each case a random anion distribution is preferred to the ordered one, but the energy differences are very small (about 4–7 kJ/mol). From the enthalpic point of view no specific anion order could be confirmed because of the very small energy differences. Detailed investigations of phase width and enthalpic stability are intensified only on cobalt oxynitride, due to the very costly calculations.

	Ordered	Random
Sc	-17.698	-17.722
Co	-14.361	-14.407

Table 6: Calculated energies (eV/f.u.) of the supercell structures with different anion arrangements of the $3d$ transition-metal oxynitrides.

The different oxynitrides $\text{CoO}_x\text{N}_{1-x}$ with varying x were calculated using non-

spin-polarized and spin-polarized approaches, but the energy differences between these were negligible (vanishing moments) such that diamagnetic (or Pauli paramagnetic) calculations turned out to be perfectly sufficient. In these supercell calculations, the unit cell parameters as well as all atomic sites were allowed to fully relax to their optimum values. While there is a loss of cubic symmetry upon relaxation/deformation and especially upon changing the oxygen/nitrogen ratio, the underlying structural principle of the zinc blende structure — fourfold coordination throughout — remains intact. The relaxation of all structural elements is most easily demonstrated by the resulting interatomic distances, for example in the form of the radial distribution function (RDF) for the combinations Co–N and Co–O, as shown in Figure 12.

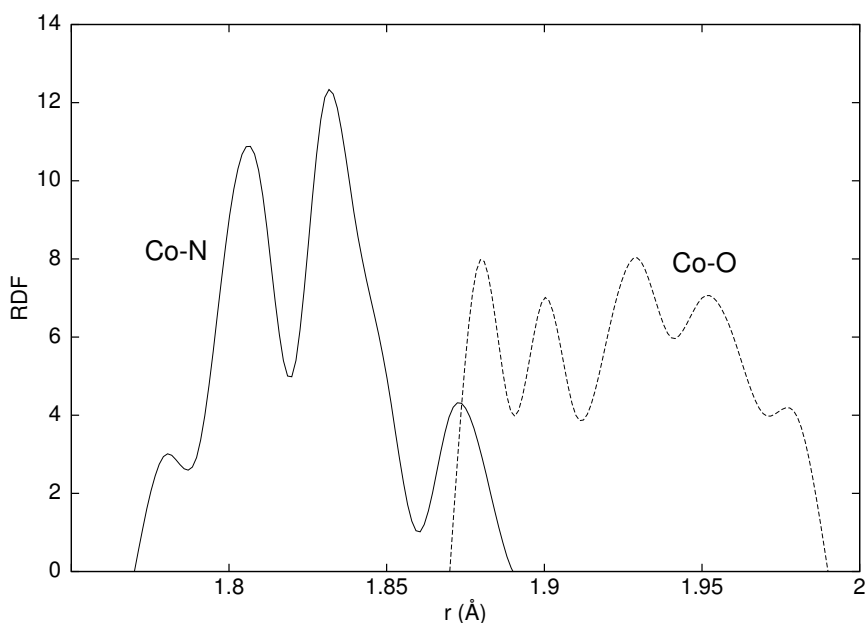


Figure 12: Radial distribution function (RDF) of the Co–N and Co–O interatomic distances in the $\text{CoO}_{0.5}\text{N}_{0.5}$; the values were extracted from a fully optimized supercell, containing 32 Co and 16 N/O atoms, and interpolated using a cubic spline.

For comparison, the Co–N and Co–O bond lengths within the zinc blende-type polymorphs of CoN and CoO are *exactly* 1.85 and 1.97 Å. Inside the randomly ordered $\text{CoO}_{0.5}\text{N}_{0.5}$ modeled by using a supercell geometry, the corresponding

spectra of interatomic distances are 1.78–1.88 Å (Co–N) and 1.88–1.98 Å (Co–O). The structural deformation itself is due to a local optimization of bonding; remember that the high-symmetry model employing identical sites for nitrogen/oxygen atoms still showed small regions of antibonding interactions close to the Fermi level (see LMTO calculations before in Figure 8). When it comes to the energetic result of the various anionic substitutions, an overview of the calculus according to Equation 1 is presented in Figure 13;

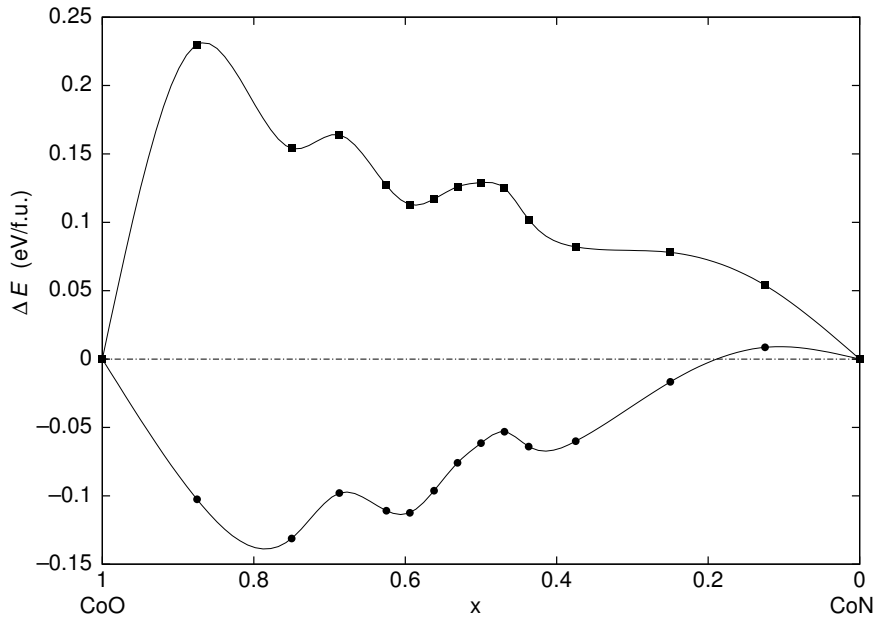


Figure 13: Theoretical ΔE - x diagram calculated for various $\text{CoO}_x\text{N}_{1-x}$ compositions according to Equation 1.

thus, negative/positive ΔE values indicate energetically stable/unstable ternary oxynitrides. To a good approximation, these energy differences may be interpreted as differences in enthalpy. The upper curve in Figure 13, in reference to the two most stable binary phases (rocksalt CoO, zinc blende CoN), manifests that any zinc blende-type compound belonging to the phase range $\text{CoO}_x\text{N}_{1-x}$ is *energetically (enthalpically) unstable* because of the positive sign of ΔE ; thus, $\text{CoO}_x\text{N}_{1-x}$ should have never been observed or isolated due to the large stability of the competing rocksalt CoO. By contrast, the lower curve of Figure 13 makes oxynitride formation immediately understandable since it stands for $\text{CoO}_x\text{N}_{1-x}$ phase formation competing with *metastable* zinc blende CoO and zinc blende

CoN. The curve suggests that a broad range of *metastable* cobalt oxynitrides with a composition range $0.1 \leq x \leq 0.7$ must be obtainable; in particular, a maximum stabilization of 10–15 kJ/mol is visible for the more oxygen-rich non-stoichiometric phases. This admittedly small energetic value can be regarded as reliable since no bond breaking/formation is involved upon comparison with the binary zinc blende phases; the energetic stabilization of $\text{CoO}_x\text{N}_{1-x}$ merely indicates the optimization of all atomic site parameters for Co, N, and O in the ternaries. Whether the three local regions of stability in the lower curve of Figure 13 are real or merely reflect the finite size of the computational model can not be determined.

In summary, the formation of $\text{CoO}_x\text{N}_{1-x}$ oxynitride materials appears to be a kinetically controlled phenomenon as long as zinc blende CoO (as opposed to rocksalt CoO) is one of the competing binary phases. This theoretical clue is backed by the experimental observation of a “thermal sensitivity” reported for $\text{CoO}_x\text{N}_{1-x}$ [70], decomposing into rocksalt CoO, metallic Co, and molecular nitrogen *at higher temperatures* (above 400 °C); CoN itself decomposes into Co and N_2 above 250 °C. Thus, it can be concluded that for moderate temperatures (kinetic control), almost any ternary $\text{CoO}_x\text{N}_{1-x}$ will be slightly preferred (see lower curve in Figure 13), in harmony with the experimental observation of a broad phase width and varying composition. Further entropy effects are not considered here, but they will slightly favor, on the order of less than 3 kJ/mol, the formation of ternary phases; this approximate value is based on a rough estimate for the ideal (configurational) entropy of mixing of $\text{CoO}_{0.5}\text{N}_{0.5}$ and a synthetic temperature of not more than 250 °C.

5. Oxynitrides of Vanadium, Niobium and Tantalum

Three decades ago, the first non-stoichiometric oxynitrides of vanadium were prepared by Brauer and Reuther [39]. The authors reported a couple of different non-stoichiometric compositions within the phase diagram V/O/N, and the crystal structure of all these compounds was identified as being the rocksalt type. More than 20 years later, detailed investigations of the electronic and magnetic properties were then performed by Wang *et al.* [79]. For example, the compound $\text{VO}_{0.5}\text{N}_{0.5}$ is characterized by an electrical resistivity of about $2 \times 10^{-3} \Omega \cdot \text{cm}$ which turns out to be weakly temperature-dependent, being typical for either a metal or a heavily doped semiconductor. Magnetic susceptibility measurements of $\text{VO}_{0.5}\text{N}_{0.5}$ show no evidence for a magnetic ordering and yield a magnetic moment of $0.25 \mu_{\text{B}}$ per vanadium atom. The small effective moment is difficult to explain keeping in mind the large effective moments of V^{2+} and V^{3+} (2.8 and $3.8 \mu_{\text{B}}$, respectively) [80], but it can be noted that $\text{VO}_{0.5}\text{N}_{0.5}$ is seemingly a metal for which the idea of large localized atomic moments is ill-fitting.

In the phase diagram of V/O/N, there is only one compound (V_2O_5) experimentally known which contains vanadium in its highest oxidation state (V^{5+}). Vanadium pentoxide is a comparatively “old” phase and was first synthesized by Ketelaar in 1936 [81]. At the present time, there are two different crystallographic phases of V_2O_5 reported [82]. In addition, electronic-structure calculations have been performed on the existence of the hypothetical phase V_3N_5 , the nitrogen analogue of V_2O_5 . The predicted structure of V_3N_5 resembles the Ta_3N_5 structure [83], but this has not been experimentally verified yet.

5.1 Stoichiometrically Precise Vanadium Oxynitride

The search for possibly stable crystallographic phases of a stoichiometrically precise VON starts with the investigation of several possible structure types [71]. The composition implies pentavalent vanadium which, as was mentioned before, is only known from V_2O_5 for the phase diagram of V/O/N. The computational search for a structurally stable VON was then carried out based on several known structure types of the composition AB_2 . The effective ionic radii of V^{5+} for tetrahedral/octahedral coordinations are 0.36 and 0.54 Å [84], and this is significantly smaller than for Nb^{5+} (0.48 and 0.64 Å) and Ta^{5+} (0.64 Å for octahedral coordination). In terms of size, V^{5+} lies between As^{5+} and Sb^{5+} such that a lowered V^{5+} coordination number is truly expected for VON. On the basis of the used total-energy DFT method, the atomic positions as well as the lattice parameters were optimized for all different structures; sometimes a loss of symmetry as well as a change in atomic coordinations are often observed. For many structure types, several different anion arrangements are possible of which only the energetically lowest ones are considered. The results of these calculations for several of the different structure types are shown in Table 7, containing the energy and volume for VON in the given structure type, and also the relative energies/volumes with respect to the lowest energy configuration. The results for all calculated structure types are shown in Table 19 (Appendix).

As expected from purely geometric (ionic radii) criteria, the results of the density-functional calculations clearly manifest the preference of V^{5+} for lower coordination numbers. In particular, a tetrahedral surrounding is the optimum choice for pentavalent vanadium; in fact, a tetrahedral polyhedron is found for the classical vanadates, with more or less regular shapes and V–O distances between 1.6 and 1.8 Å, coinciding with the sum of the ionic radii [84]. Table 7 also reflects that the different polymorphs of VON exhibit grossly varying molar volumes, and the lowest volumes are found for the highest coordination numbers, as predicted by the pressure-coordination rule proposed by Neuhaus [85]. In order to derive a volume standard for one formula unit (f.u.), an expected volume of VON may be computed as the arithmetic average of the volumes of

Structure type	cn	E_0	V_0	ΔE	ΔV
α -Cristobalite	4	-26.209	68.35	0	0
α -Quartz	4	-26.153	55.22	0.056	-13.13
Anatase	6	-26.063	32.85	0.146	-35.50
Baddeleyite	7	-25.977	27.62	0.232	-40.73
Rutile	6	-25.913	31.78	0.296	-36.57
Fluorite	8	-24.806	27.10	1.403	-41.25

Table 7: Structure type, coordination number of the vanadium atom (cn), total energy (E_0) and volume (V_0) at zero pressure, relative energy (ΔE) and relative volume (ΔV) with respect to the lowest-energy configuration for several hypothetical polymorphs of VON. Energies are given in eV and volumes in \AA^3 per formula unit VON.

V_2O_5 and (still hypothetical) V_3N_5 :

$$V(\text{VON}) = \frac{1}{5} [V(\text{V}_2\text{O}_5) + V(\text{V}_3\text{N}_5)] = \frac{1}{5} V(\text{"V}_5\text{O}_5\text{N}_5\text{"})$$

This arrives at 32.6 \AA^3 per formula unit of VON, suggesting that the structure types with tetrahedral coordination (see Table 7) are somewhat loosely packed.

For a more complete picture, it is worthwhile investigating how the theoretical polymorphs from Table 7 respond when pressure is applied. The technical details of this approach are shown in Appendix A. All the calculated polymorphs show a more or less regular pressure-energy dependence, except for the baddeleyite type. Surprisingly, these calculations result in *two* stable structures. The first one corresponds to the original baddeleyite structure whereas the other is a strongly distorted variant of it. The energy of this distorted form of baddeleyite is -26.157 eV/f.u. , which is almost 0.2 eV/f.u. lower in energy than the regular baddeleyite structure. The complete energy-volume dependence of these two VON phases is plotted in Figure 14. Here, not only two but *four* crystallographic phases show up. The additional two structures are high-pressure phases which, however, do *not* possess a well-defined equilibrium volume and may therefore be

considered essentially unstable under whatever conditions. Starting with the distorted baddeleyite structure (I) on the right (open squares) which has the largest volume and the lowest energy, a compression leads to the regular baddeleyite structure (II) which appears at a slightly higher energy and smaller volume. Upon compressing the structure even more, the monoclinic cell of baddeleyite (II) changes into an orthorhombic cell (III) (filled squares).

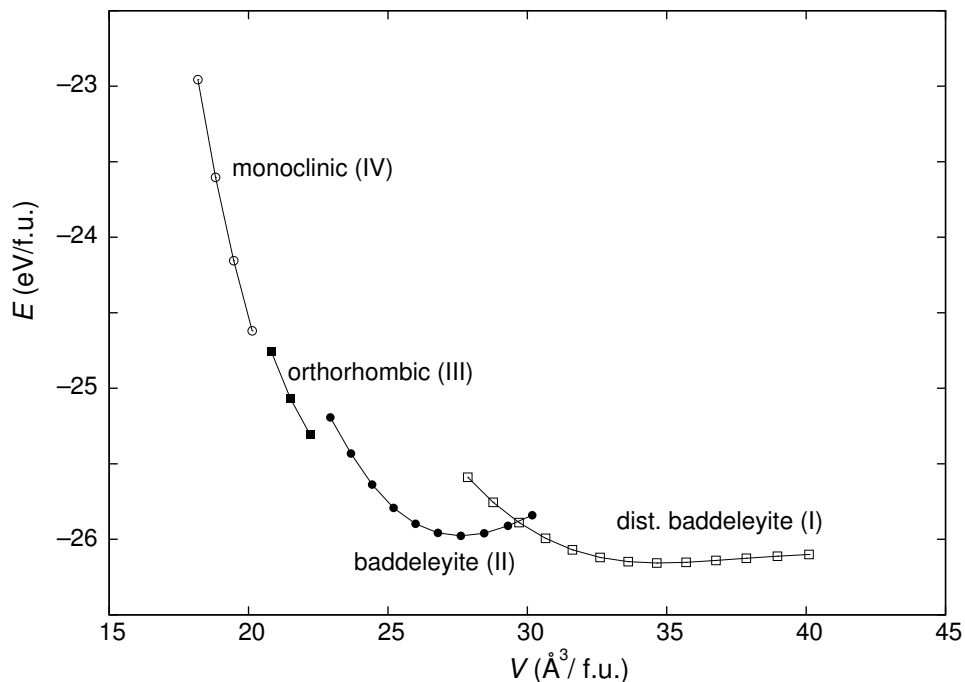


Figure 14: Energy-volume diagram of VON with four baddeleyite-related structures.

In the region of highest pressure (smallest volumes, open circles), the orthorhombic cell (III) changes back into a monoclinic cell (IV), and the structural formation of N_2 dimers can be observed. The N–N bond length of 1.34 \AA is between those of O=O (1.21 \AA) and F–F (1.42 \AA) but much larger than in the uncharged $\text{N}\equiv\text{N}$ molecule (1.10 \AA). Thus, the presence of an N_2^{2-} species is indicated which, in turn, reflects an *internal redox competition* yielding trivalent vanadium, qualitatively corresponding to $(\text{V}^{3+})_2(\text{O}^{2-})_2(\text{N}_2^{2-})$. In fact, the coordination number of vanadium increases to eight, and V^{3+} forms doubly capped distorted trigonal prisms. Similar pernitride anions were reported by Kniep *et al.* in the solid state structures of SrN_2 [86] and BaN_2 [87]. The experimental

bond length of the double-bonded N_2^{2-} in both structures, however, is around 1.22 \AA . The comparison with the theoretical bond length of 1.34 \AA as found for the N_2 dimer in the VON structure (see Figure 15, left) evidences that the N atoms are higher charged resulting in a N–N bond somewhere between a single and a double bond.

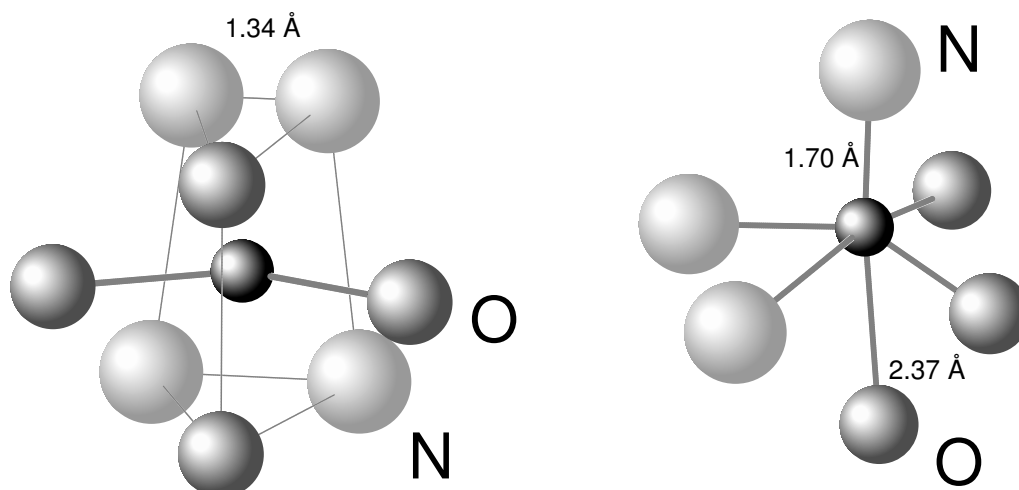


Figure 15: Left: Doubly capped distorted trigonal prism predicted as the vanadium coordination in the unstable high-pressure monoclinic structure (IV). Right: Distorted octahedron predicted as the vanadium coordination in the distorted baddeleyite structure (I).

Although the distorted baddeleyite structure is not the energetically lowest configuration, its volume of $34.65 \text{ \AA}^3/\text{f.u.}$ also matches much better with the one derived from V_2O_5 and V_3N_5 ($32.6 \text{ \AA}^3/\text{f.u.}$). Within distorted baddeleyite, the vanadium atom is surrounded by 1+4+1 anions which form a distorted octahedral arrangement. These octahedra are connected by sharing edges. The distinguishing feature of this polyhedron is a single apical double-bonded nitrogen at a distance of 1.70 \AA and four more or less coplanar anions (N,O) in the base at distances of $1.79\text{--}2.17 \text{ \AA}$. Another oxygen atom is situated at the opposite position of the short V–N bond and forms a weak 2.37 \AA long V–O bond (see Figure 15, right). Several different anionic arrangements are possible within this distorted structure, at least in principle, but it appears that only one ordered configuration is energetically stable. Despite the fact that the dis-

torted baddeleyite structure has been computationally derived from the regular one, there are large differences in interatomic geometries, easily visible from a look along the monoclinic axis given in Figure 16. The two small arrows denote the direction of which pressure is applied on the unit cell of VON in the regular baddeleyite structure, leading to the distorted baddeleyite structure.

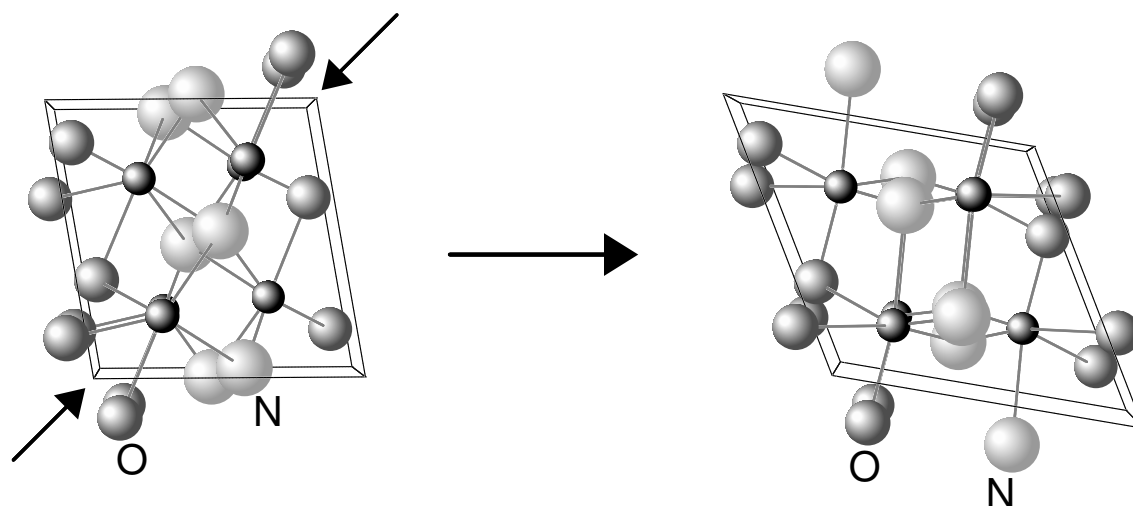


Figure 16: Unit cell of vanadium oxynitride in the regular baddeleyite structure (left) and in the distorted baddeleyite structure (right).

One may ask for the reason of having investigated the regular and distorted baddeleyite structure type although both are *not* the energetically lowest structures. The clue is found in the thermochemistry of VON, and its synthesis may proceed by the reaction given below:



In general, a successful high-pressure synthesis requires that the volume of the products must be smaller than the volume of the reactants. Moreover, the energy differences between them should be so small that it can be compensated by applying pressure. In Table 8 the energies and volumes of the reactants and also of VON in several different structure types are listed. The energy and volume differences (ΔE , ΔV) refer to the energy and volume of the reactants V_2O_5 , VN and N_2 at absolute zero temperature.

	E	V	ΔE	ΔV
Educts	-132.41	200.40	0	0
α -Cristobalite	-131.05	341.75	1.36	141.35
distorted Baddeleyite	-130.79	173.25	1.62	-27.15
α -Quartz	-130.77	276.10	1.64	75.70
Baddeleyite	-129.89	138.10	2.52	-62.30
Rutile	-129.57	158.90	2.84	-41.50
Fluorite	-124.03	135.50	8.38	-64.90

Table 8: Comparison of the energies and volumes of the educts ($V_2O_5 + 3 VN + N_2$) and products (5 VON in several different structure types) according to Equation 1. The energies (E) and energy differences (ΔE) are given in eV. The volumes (V) and the volume differences (ΔV) are given in \AA^3 .

Clearly, the high-pressure synthesis of VON may only succeed if ΔV (see Table 8) is negative. Therefore, VON in the α -cristobalite structure can *not* be obtained although it exhibits the lowest energy. The same is true for the α -quartz structure of VON. For the moment, the distorted baddeleyite structure appears to be the energetically lowest polymorph which can be achieved by a high-pressure synthesis according to Equation 1. To determine the influence of the pressure on the chemical equilibrium and the Gibbs energy G , one first needs to calculate the energy-volume dependence for all the polymorphs. The pressure p is then obtained by differentiation of a Murnaghan fit of the energy-volume diagram. Finally, the enthalpies are calculated according to $H = E + pV$, where E stands for the total energy. The reason for having been able to replace the Gibbs energy G by the enthalpy H through a removal of the TS term in the Gibbs–Helmholtz equation is easy to understand: to a very good approximation, the entropic contributions of solid-state materials are negligible, and the same is true for molecular nitrogen at absolute zero temperature. Under these condi-

tions, the derived enthalpy is a reliable indicator for the stability of a structure type with respect to the applied pressure. The enthalpies are plotted *relative* to the ones of the reactants (Equation 1, $V_2O_5 + 3 VN + N_2$) and are shown in Figure 17.

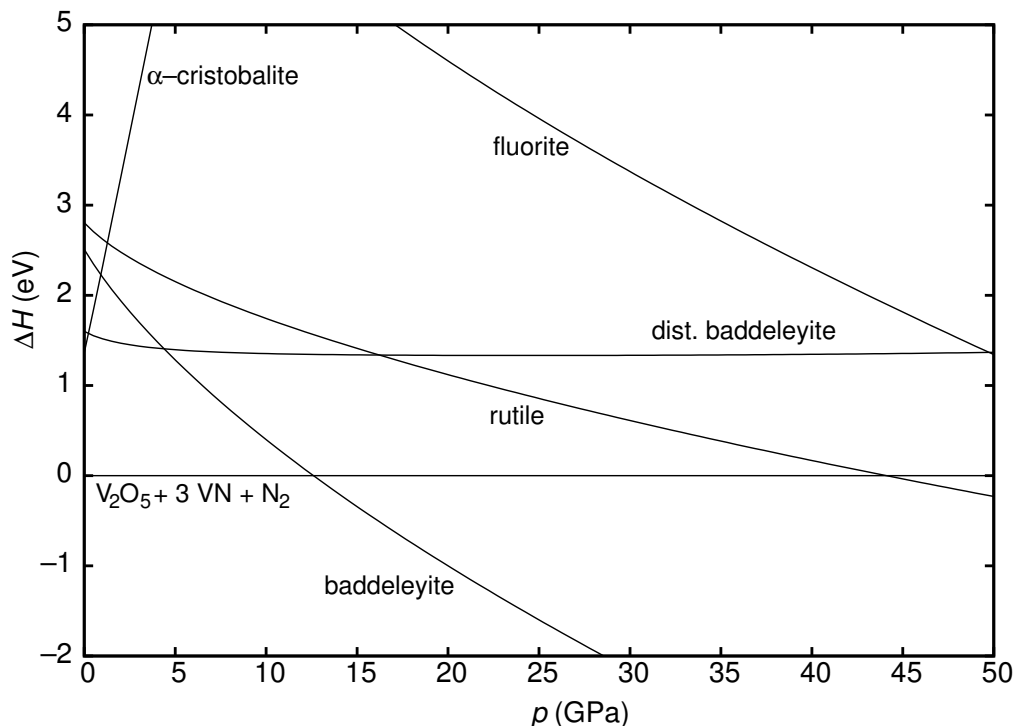


Figure 17: Theoretical enthalpy-pressure diagram for VON.

A pressure-induced synthesis of VON is predicted at about 12 GPa where VON does not adopt the expected distorted baddeleyite structure but the *regular* baddeleyite structure! This surprising result can be explained by the different compressibilities of both structures. While VON in the baddeleyite structure can be compressed more easily, the distorted baddeleyite structure is much stiffer. Again, these results are in nice accord with the pressure-homologue rule of Neuhaus stating that, under pressure, a compound adopts the structure of its higher homologues (TaON, NbON) [85].

A final electronic-structure calculation of the baddeleyite structure is performed by LMTO theory (GGA), shown in Figure 18. The density-of-states with the $3d$ contributions of vanadium are given on the left, and the COHPs of the shortest V–V, V–O and V–N bonds are shown at the right. There are

weak antibonding V–V COHPs in the valence bands, indicator of the repulsive cation–cation interactions, but the structure is held together by strong V–O/N bonds, as indicated by the bonding V–O/N COHPs below the Fermi level.

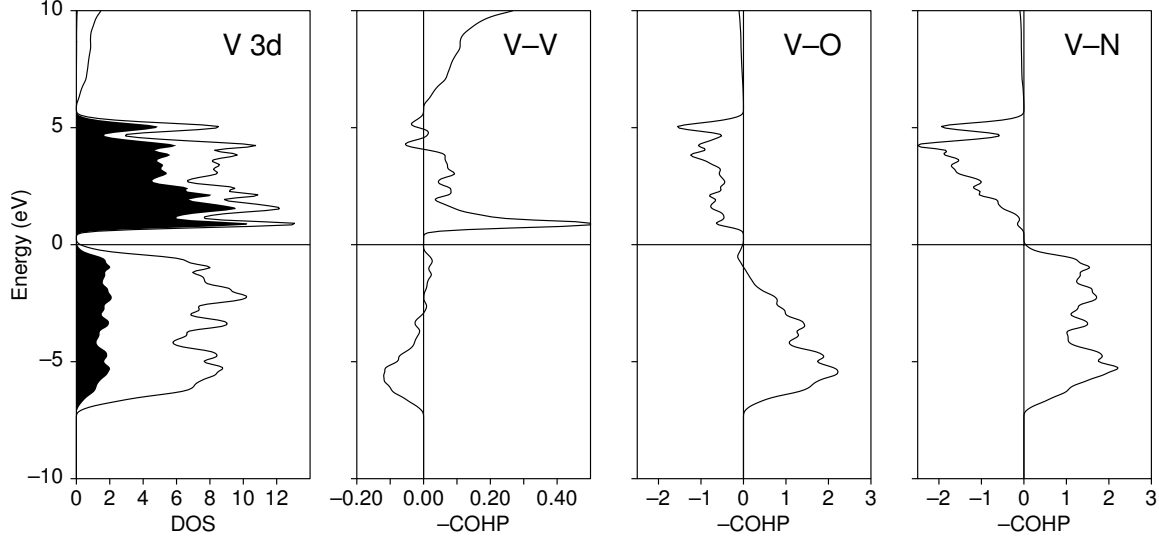


Figure 18: Density-of-states of VON in the baddeleyite structure with local $3d$ projections and crystal orbital Hamilton populations (COHP) for the V–V, V–O and V–N interactions.

Within the baddeleyite structure of VON, the vanadium atom is surrounded by three oxygen atoms and four nitrogen atoms. Summing up the integrated COHPs for each of these interactions, the V–N bond (0.195 eV/bond) turns out slightly stronger than the V–O bond (0.162 eV/bond). The dispersion of the bonding V–N interactions up to the Fermi level is wider than the V–O dispersion, which obviously expresses the more covalent nature of the V–N bond. The calculated bandgap of 0.6 eV is very small, and it is mainly determined by filled nitrogen states just below the Fermi level (highest occupied crystal orbitals) and by empty vanadium states in the lowest unoccupied crystal orbitals.

5.2 Niobium Oxynitride

In 1954, Nils Schönberg discovered the first non-stoichiometric niobium oxynitrides [88]. He found two metallic ternary phases; $\text{NbO}_{0.1}\text{N}_{0.9}$ with the NaCl

structure and $\text{NbO}_{0.3}\text{N}_{0.6}$ with a tetragonally distorted NaCl structure. The synthesis of several non-stoichiometric niobium oxynitrides is also reported [89–92]. Stoichiometric NbON was first synthesized by Buslaev, and it adopts the baddeleyite structure as shown in Figure 16 (left). A detailed description of this structure type is given in the next section. This chapter is mainly focused on the geometric as well as the and electronic structure of NbON and presents the first theoretical investigations of NbON. Pseudopotential-GGA calculations are performed on NbON in the baddeleyite structure. The results are shown in Table 9. The calculated lattice parameters and atomic coordinates match very

	Experimental [93]			Calculated		
Lattice parameters (\AA , $^\circ$)						
a	4.970(3)			5.029		
b	5.033(3)			5.077		
c	5.193(3)			5.243		
β	100.23			100.07		
Volume ($\text{\AA}^3/\text{f.u.}$)	31.96			32.95		
Positions	x	y	z	x	y	z
Nb ($4e$)	0.2911(1)	0.0472(1)	0.2151(1)	0.294	0.049	0.219
O ($4e$)(A2)	0.0636(8)	0.3244(8)	0.3476(9)	0.062	0.323	0.350
N ($4e$)(A1)	0.4402(8)	0.7546(11)	0.4782(9)	0.442	0.755	0.477

Table 9: Experimental and theoretical structure data of NbON on the basis of pseudopotential-GGA calculations.

well with the experimental ones. The calculated volume is a little too large but this is a well known feature of the generalized gradient approximation (GGA). Within this structure type there are several different anion arrangements possible. These various combinations are calculated and the results are shown in Table 10. The position denoted as A1 is the 'nitrogen' position from Table 9. The last entry from Table 10 corresponds with the structural data from Table 9.

In good agreement with the experimental results, these calculations show a

Position = Occupation	Energy	Volume
A1=4× O	0.335	34.06
A1=1× N; 3× O	0.355	33.60
A1=2× N; 2× O	0.261	33.22
A1=3× N; 1× O	0.173	33.16
A1=4× N	0	32.95

Table 10: Theoretical total energies and volumes of NbON as a function of anionic ordering on the basis of pseudopotential-GGA calculations; the lowest relative energy (denoted with 0 eV/formula unit) corresponds to a total energy of -28.541 eV/f.u. and the volume is in $\text{\AA}^3/\text{f.u.}$.

clear preference of one specific anion order, which is at least 16.7 kJ/mol lower in energy than the other distributions. Moreover, this energy difference is much larger than the differences calculated for the $3d$ transition-metal oxynitrides, which are around 4–7 kJ/mol. Therefore the anions have fixed positions within the baddeleyite structure of NbON.

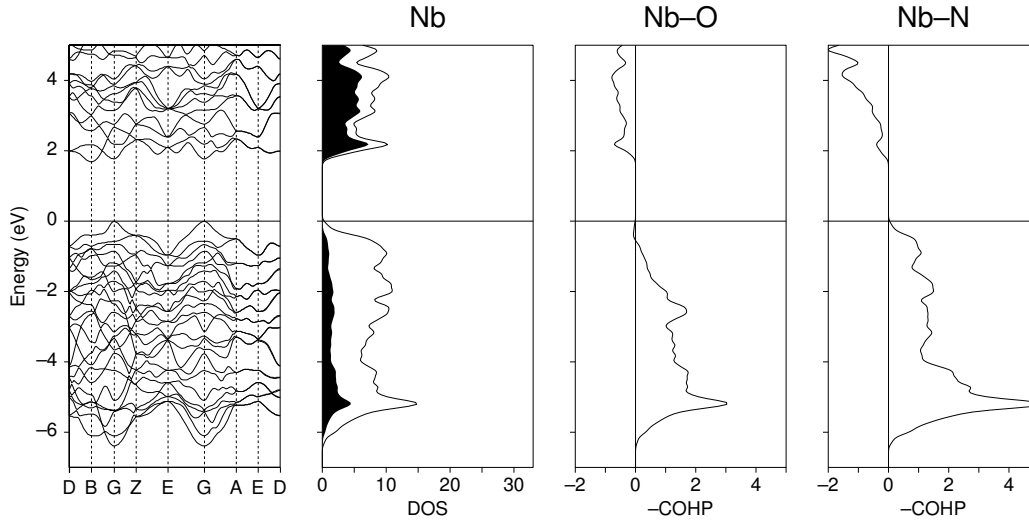


Figure 19: Band structure, density-of-states (DOS) with local Nb contributions in black, and Crystal Overlap Hamilton Population (COHP) of the Nb–O and Nb–N bonds in NbON calculated with the TB-LMTO-ASA method using the LDA.

NbON is experimentally described as a blue-colored semiconductor. Electronic structure calculations are performed using LMTO, to investigate if the bandgap is correctly calculated. (see Figure 19) The band structure calculations result in an indirect bandgap of ca. 1.7 eV, which is mainly caused by nitrogen contributions just below the Fermi level and niobium contributions at the bottom of the conduction band. The COHP calculations show that the covalent Nb–O interactions are smaller than the Nb–N interactions. Consequently the Nb–O interactions are more ionic than the Nb–N bonds.

5.3 Tantalum Oxynitride

The very first investigations of the ternary system Ta/O/N were performed by Schönberg almost half a century ago [94]. Schönberg described four non-stoichiometric phases with different O:N ratios, namely $\text{TaO}_{0.10}\text{N}_{0.90}$, $\text{TaO}_{0.25}\text{N}_{0.75}$, $\text{TaO}_{0.35}\text{N}_{0.65}$, and $\text{TaO}_{0.50}\text{N}_{0.50}$. Eleven years later, another two tantalum oxynitrides were published by Brauer et al. [67, 68] and by Buslaev et al. [95] almost coincidentally. These two TaON polymorphs contain pentavalent Ta and an equal O:N ratio, *i.e.*, they are stoichiometrically precise.

The first phase, β -TaON reported by Brauer et al. [67, 68] crystallizes in the monoclinic system and is iso-structural with baddeleyite (ZrO_2). Here, the tantalum atom experiences sevenfold coordination by three oxygens (1.99–2.15 Å) and four nitrogens (2.07–2.15 Å). Together they form mono-capped, twisted trigonal prisms which are staggered to form zigzag layers [96]. The beautiful simplicity is best appreciated by noting the TaO_3N_4 prisms as shown in Figure 20. Synthetically, β -TaON was found as an intermediate in the synthesis of Ta_3N_5 from Ta_2O_5 using ammonia. Nevertheless, the phase can also be made by inserting oxygen into the nitrogen network of Ta_3N_5 . This tuning of the bandgap by changing the O:N ratio ($3 \text{O}^{2-} \cong 2 \text{N}^{3-}$) has already been mentioned in the introductory section.

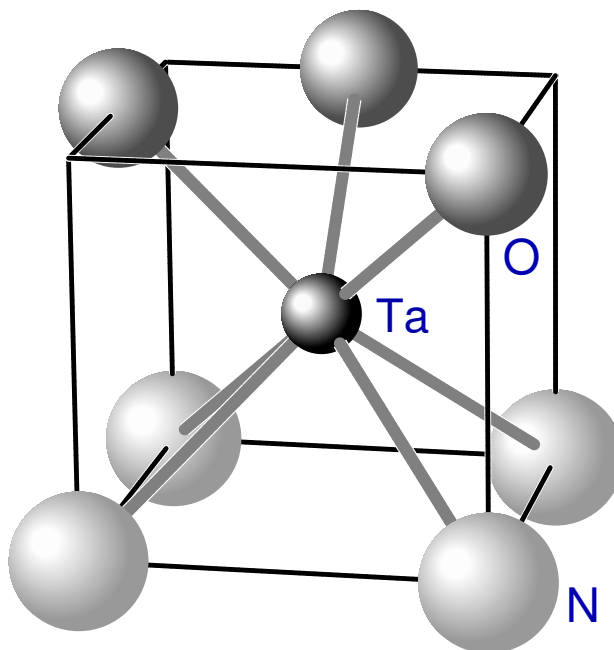
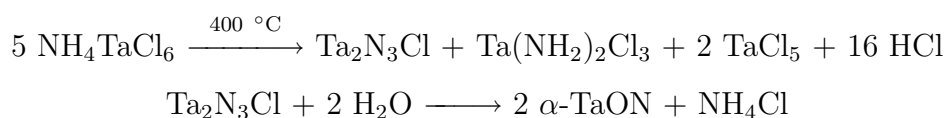


Figure 20: The mono-capped TaO_3N_4 prisms within the β -TaON structure.

The preference for a specific anionic order inside β -TaON has been confirmed by Armytage and Fender using powder neutron diffraction [93]. Recent first-principles calculations performed on β -TaON are in nice agreement with these experimental results [97,98]. Only in 2002, however, it was found that the supposedly intrinsic green color of β -TaON was caused by an impurity in the oxide precursor which was contaminated with a little Nb_2O_5 [99]. Under the reaction conditions, niobium oxide also incorporates nitrogen atoms and then forms a black $\text{Nb}(\text{O}_x\text{N}_y)$ phase. The interference of this black contamination with the actual *yellow* color of β -TaON lets us rationalize the green color originally mentioned by Brauer et al.

The other low-temperature polymorph, α -TaON, has been reported to adopt a more complicated hexagonal structure (see Figure 21), and it was first prepared by Buslaev et al. [95,100]. According to the authors, the first synthetic step is the decomposition of NH_4TaCl_6 at 400 °C which leads to $\text{Ta}_2\text{N}_3\text{Cl}$. Then, a red powderous phase, α -TaON, is obtained by the hydrolysis of this nitrile chloride:



Despite this relatively simple synthesis, neither the nitrile chloride nor α -TaON was reproduced by the competing group of Brauer et al. in subsequent publications [68, 101].

According to the Buslaev et al., both compounds (tantalum nitrile chloride and α -TaON) were characterized by powder X-ray diffraction and infrared spectroscopy [95]. White — not red! — single crystals of α -TaON were obtained by a transport reaction of powderous α -TaON with NH_4Cl . The best crystals (size: 2–4 mm) grew in temperature gradients from 900–1000 °C and 1000–1100 °C, and these crystals exhibited hexagonal symmetry. A first crude crystallographic analysis resulted in space group $P6/mmm$ and cell parameters $a = 4.21 \text{ \AA}$ and $c = 4.04 \text{ \AA}$. Tantalum is situated at the origin whereas either O or N are stochastic located at $0\ 0\ \frac{1}{2}$ (see Figure 21, top). Because of the chosen symmetry, no other anion could be positioned, which trivially leads to the false composition $\text{TaN}_{0.50}\text{O}_{0.50}$. This phase, however, seems to be different from the non-stoichiometric one found by Schönberg in 1954.

A more elaborate analysis on a better-shaped single crystal gave evidence for a superstructure. It is also characterized by a hexagonal cell and space group $P6/mmm$ but it exhibits a *tripled* volume ($a = 7.31 \text{ \AA}$, $c = 4.04 \text{ \AA}$). Small satellites around the Bragg peaks indicated the possibility of an even more complex structure such as the antigorite type [102]. Nevertheless, in this best structural model the tantalum atoms are located on two crystallographic different positions, namely on $1a$ ($0\ 0\ 0$) and on $2c$ ($\frac{1}{3}\ \frac{2}{3}\ 0$). The anionic sites for O and N were given as $1b$ ($0\ 0\ \frac{1}{2}$) (**A1**), $2d$ ($\frac{1}{3}\ \frac{2}{3}\ \frac{1}{2}$) (**A2**), and $3f$ ($\frac{1}{2}\ 0\ 0$) (**A3**) as shown in Figure 21, bottom. While the metal/nonmetal composition is in harmony with the formula TaON, the precise spatial distribution of the anions O/N over the above sites could not be clarified because of the insensitivity of the X-ray technique to this question.

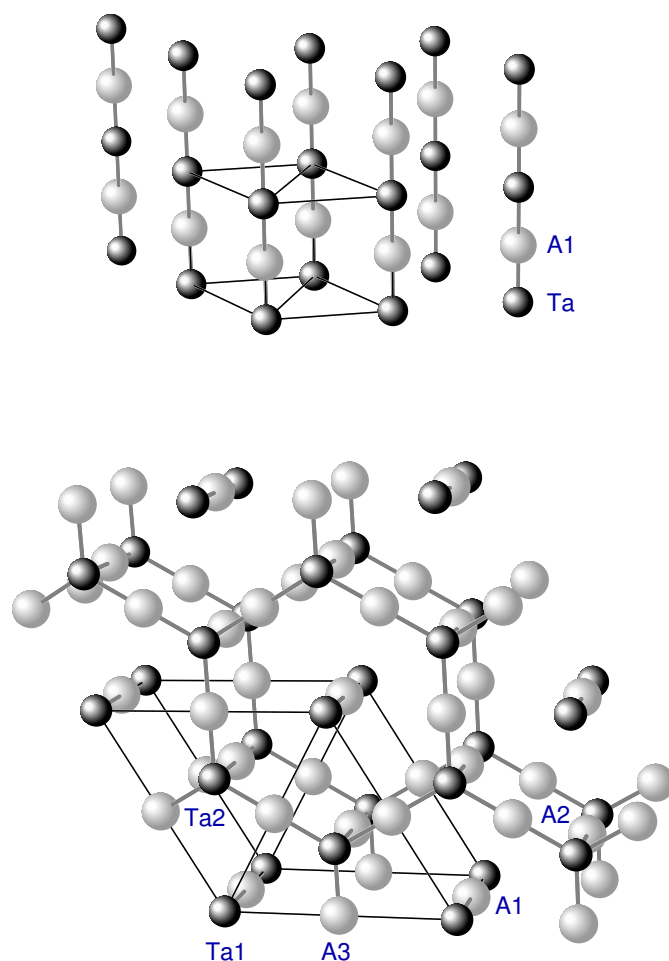


Figure 21: Crystal structures for α -TaON derived from single crystals, with the first approximate proposal shown at the top and the more elaborate one, correctly corresponding to the ideal TaON composition, at the bottom. The latter structure report, with oxygen/nitrogen atoms situated at Wyckoff positions $1b$, $2d$, and $3f$, is part of the Inorganic Crystal Structure Database (entry number 20321).

In this detailed α -TaON structure drawn in Figure 21 (bottom), the Ta2 atom is coordinated by five anions in a trigonal bipyramidal arrangement. The Ta2–A2 and Ta2–A3 bond lengths of 2.02 and 2.11 Å are quite similar to the distances found in β -TaON (Ta–N: 2.06–2.15 Å, Ta–O: 1.99–2.15 Å). The other tantalum atom, Ta1, exhibits an unusual twofold, 2.02-Å- σ -coordination by two A1 anions which was already part of the simpler substructure (see Figure 21, top). Being aware of that sub-coordination, Buslaev et al. proposed a further

saturation of the coordination sphere of Ta1 by the six nearest A3 atoms, which would eventually lead to an eightfold (2+6) coordination. Nonetheless, the Ta1–A3 distances (3.66 Å) seem to be fairly large, much larger than in the ϵ -TaN structure [103] where similar features of second-nearest neighbor coordination are also found, but with Ta–N = 2.66 Å.

5.3.1 β -TaON

The first electronic structure calculations on β -TaON have already been performed by de Width et al. [97] using density-functional theory. The results concerning β -TaON match very well with theirs, and both are in excellent, if not superb agreement with the experimental values; for numerical data, see Table 11.

	Experimental [93]			Calculated		
Lattice parameters (Å, °)						
a	4.9581(5)			4.99		
b	5.0267(6)			5.05		
c	5.1752(6)			5.20		
β	99.640(7)			99.80		
Volume (Å ³ /f.u.)	31.79			32.30		
Positions	x	y	z	x	y	z
Ta (4e)	0.292(1)	0.046(1)	0.213(1)	0.294	0.046	0.215
O (4e)	0.064(1)	0.324(1)	0.345(1)	0.063	0.328	0.346
N (4e)	0.4449(8)	0.7566(9)	0.4810(8)	0.442	0.744	0.481

Table 11: Experimental and theoretical structure data of β -TaON on the basis of pseudopotential-GGA calculations.

The difference between experiment and theory seems to be almost negligible, in the case of the spatial parameters falling into the uncertainty range indicated by the experimental standard deviations. The theoretical volume per formula unit is a little larger (1.5%) than the experimental number, but this slight overestimation of the volume is a well-known feature of the GGA functional. The preference of the given anionic order deduced from neutron diffraction can also be confirmed by the present calculations, namely by explicit calculations of the energies of all possible anionic arrangements. The experimentally observed ordered distribution, as numerical given in Table 11, is 0.65–1.71 eV lower in energy than all the others.

Touching upon optical properties, measurements of diffuse reflectance spectra on β -TaON were carried out by Orhan et al. and resulted in a (direct) bandgap of 2.4 eV [99]. These electronic structure calculations performed with the FLAPW method and the GGA functional yield a theoretical value of 2.1 eV for the direct bandgap, which reflects the DFT-typical underestimation. The close correspondence between experiment and theory is surprising and should not be overinterpreted since ground-state DFT calculations cannot be used in terms of properties that are due to excited states.

For the sake of completeness, the electronic structure —also by means of the LMTO method— has been recalculated in order to investigate the bonding situation within β -TaON using the Crystal Overlap Hamilton Population technique (COHP) [31]. The results, based on the local-density approximation (LDA), turned out to be so similar to the preceding GGA calculations that no switch over to LMTO/GGA calculations was necessary but show them as they are. An overview of this LDA band structure, density-of-states and COHP curves is presented in Figure 22.

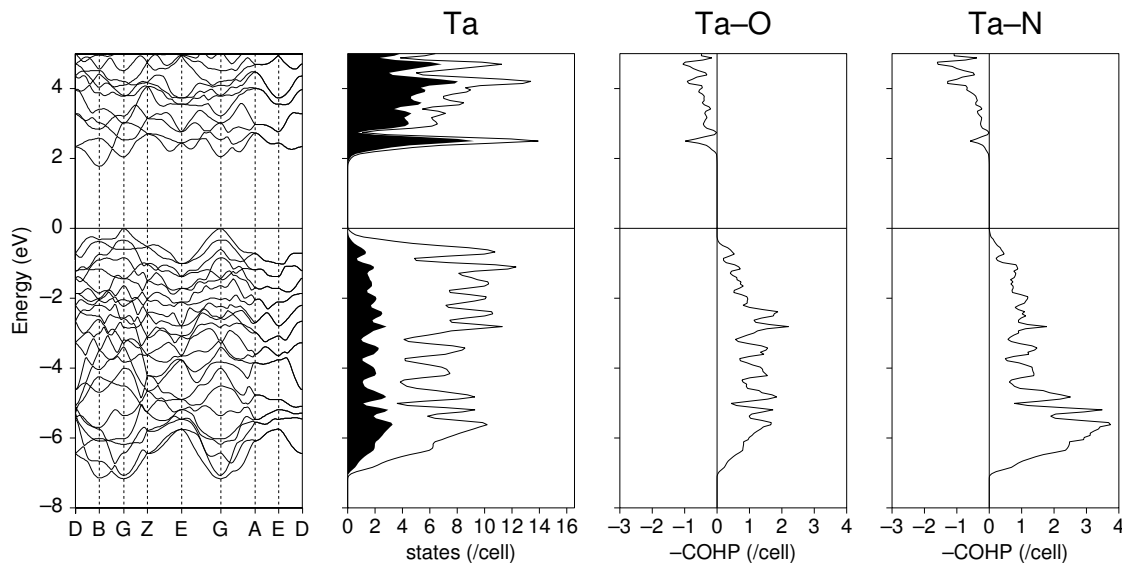


Figure 22: Band structure, density-of-states (DOS) with local Ta contributions in black, and Crystal Overlap Hamilton Population (COHP) of the Ta-N and Ta-O bonds in β -TaON calculated with the TB-LMTO-ASA method using LDA.

The calculations yield the (expected) result that the stability of β -TaON goes back to perfectly optimized Ta-O and Ta-N bonding up to the top of the valence band. The COHPs also show that the Ta-O bonding dispersion is slightly more narrow (ca. 5%) than the Ta-N dispersion, in harmony with the less covalent bonding of the O atom. Also, it is obvious that the Ta-N bond strength is higher than for the Ta-O combination; there are four equal Ta-N bonds, summing up to an integrated COHP (ICOHP) of -0.817 eV or, alternatively, -0.204 eV per single Ta-N interaction. For the Ta-O combination, there are three nearest-neighbor interactions amount to an ICOHP of -0.463 eV, that is, -0.154 eV per Ta-O pair.

The band structure plot itself reflects a smaller, indirect LDA bandgap of 1.76 eV, whereas the direct LDA bandgap is 2.02 eV, still very close to the experimental value and to the FLAPW/GGA result. As a conclusion, the agreement between theoretical and experimental results for β -TaON is just excellent taking into account that oxynitrides must be considered phases in which electronic correlation may play a major role. Still, common DFT parameterizations perform

astonishingly well.

5.3.2 α -TaON

At the beginning, the first aim was to theoretically clarify the experimentally unsolved question of anionic order. Total-energy calculations on two ordered α -TaON structures using space group $P6/mmm$ were performed. The first structure contains the oxygen atoms at the $1b$ and $2d$ Wyckoff positions and the nitrogen atoms at the $3f$ positions; in the second one, the atomic sites are simply reversed. In addition, several total-energy calculations on α -TaON with more different anionic distributions were carried out, *i.e.*, corresponding to space groups which are lower in symmetry but probably undistinguishable from each other by a simple X-ray diffraction experiment. In order to speed up the calculations, all the atomic sites were allowed to adopt the energetically most favorable coordinates, but the — probably fairly reliable — lattice parameters were held constant. The numerical results of these calculations are given in Table 12.

Symmetry	($1b$)	($2d$)	($3f$)	Energy (eV/f.u.)
$P6/mmm$	$1 \times O$	$2 \times O$	$3 \times N$	0.139
$P6/mmm$	$1 \times N$	$2 \times N$	$3 \times O$	0.739
$P2/m$	$1 \times O$	$2 \times N$	$2 \times O, 1 \times N$	0.654
$P2/m$	$1 \times N$	$2 \times O$	$2 \times N, 1 \times O$	0.000
Pm	$1 \times O$	$1 \times O, 1 \times N$	$2 \times N, 1 \times O$	0.353
Pm	$1 \times N$	$1 \times O, 1 \times N$	$2 \times O, 1 \times N$	0.309

Table 12: Theoretical total energies of α -TaON (lattice parameters fixed) as a function of anionic ordering on the basis of pseudopotential-GGA calculations; the lowest relative energy (denoted with 0 eV/formula unit) corresponds to a total energy of -26.788 eV/f.u..

The tabular entries manifest that the supposedly hexagonal α -TaON, for its given lattice parameters, must be lower in symmetry since at least one alternative structure with an ordered arrangement of O and N atoms is truly lower in energy. In order to investigate this structure in more detail, the original structure (entry number 1 in Table 12 with space group $P6/mmm$) was optimized and the energetically most favorable one (entry number 4 with space group $P2/m$) in terms of all structure parameters. That is to say, a further optimization (energy minimization) was performed by also allowing for an adjustment of the lattice parameters besides the atomic positions. The numerical results of these optimizations are given in Table 13.

	Experimental	Calculated	
Space group	$P6/mmm$	$P6/mmm$	$P2/m$
Volume ($\text{\AA}^3/\text{f.u.}$)	62.32	50.00	49.85
Energy (eV/f.u.)		-27.62	-27.79

Table 13: Experimental and theoretically optimized volumes/energies for α -TaON on the basis of pseudopotential-GGA calculations.

For these complete optimizations, the low-symmetry structure is being somewhat lower in energy than the high-symmetry one. In both cases, however, the calculated volumes are almost *twenty percent smaller than the experimental one*, a consequence of strongly shortened lattice parameters. This huge difference cannot be explained by a shortcoming of the used functional but points into another direction. For example, upon comparing the molar volume of the well-characterized β -TaON (ca. 32 \AA^3) with the various ones for α -TaON given in the above Table (ca. $50\text{--}62 \text{ \AA}^3$), the value for the α phase seems to be unacceptably large, giving a first hint for the implausibility of its structure. Still taking the (almost) hexagonal structure of α -TaON seriously, Figure 23 shows the oxygen/nitrogen-ordered optimized structure lowest in energy. The original structural idea of α -TaON is unchanged, namely a layer structure composed of linearly two-coordinate Ta1 and five-coordinate (trigonal bipyramid) Ta2.

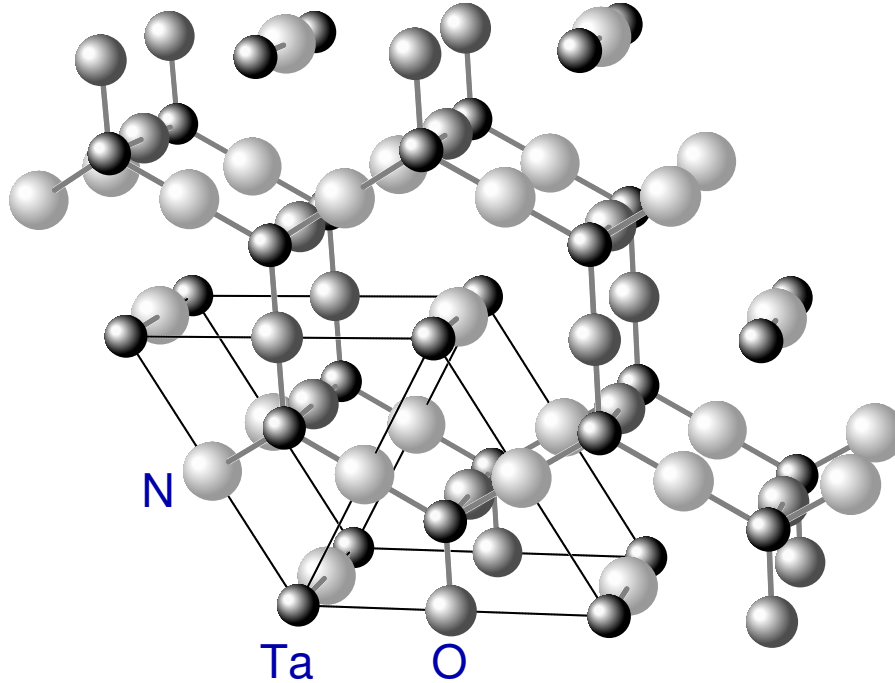


Figure 23: Energetically mostly favored anionic arrangement calculated for α -TaON on the basis of pseudopotentials and the GGA.

A preference for linear Ta–N chains and for a trigonal bipyramid that is built by two nitrogens in the plane and another three oxygens (see Figure 23) is observed, thereby breaking the space group symmetry due to the special site $3f$. Despite the too large molar volume, the calculated planar Ta–O/N distances of 1.90/1.93 Å are significantly shortened in comparison with the experimental (or theoretical) values found for β -TaON (Ta–O: 1.99–2.15 Å, Ta–N: 2.06–2.15 Å). Reconsidering that α -TaON was experimentally reported to be an insulator or semiconductor (red powder, colorless single crystals), one should expect a significant bandgap in the electronic structure. In order to stick to the experimental data as close as possible, the experimental structure of α -TaON (ICSD entry 20321, space group $P6/mmm$) for the density-of-states calculations based on

the most accurate method (Wien2k, GGA) were used. This result, including the local projections of tantalum, nitrogen, and oxygen given in black, is plotted in Figure 24.

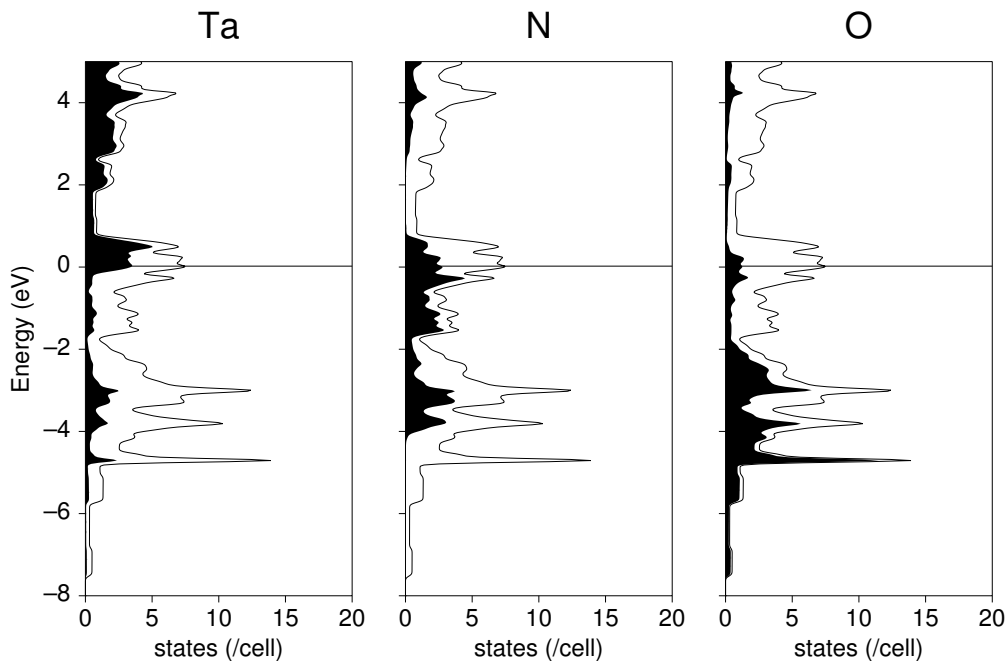


Figure 24: Theoretical density-of-states (DOS) of α -TaON, including tantalum, nitrogen and oxygen projections in black, on the basis of FLAPW and the GGA.

Surprisingly, the experimentally communicated α -TaON turns out to be a *metal* and does not show any bandgap at all, which is in total conflict with either a red or colorless solid. Although it is well-known that DFT systematically underestimates bandgaps [104], at least a small bandgap and certainly not a high DOS at the Fermi level, mostly caused by Ta and N, should be expected. Without any doubt, theory and experiment do not at all match for α -TaON.

In a last attempt to question the experimental structure of α -TaON, a diffraction diagram [105] simulated, using the experimentally reported lattice and spatial parameters given by Buslaev et al. [95], ICSD entry 20321, which itself is based on the structure determination performed on a single crystal. Very fortu-

nately, the authors also supplied an experimental powder diffraction diagram in their original communication but which probably corresponds to the bulk phase, not necessarily to the single crystal investigated. Both diagrams are presented together in Figure 25.

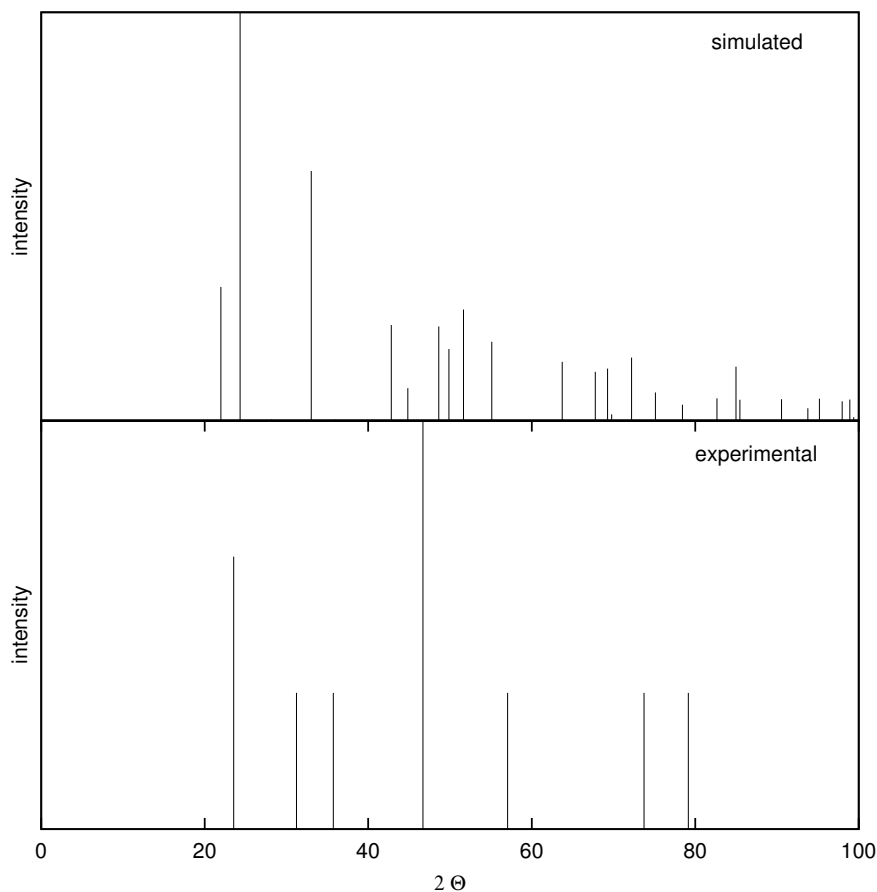


Figure 25: Experimentally reported diffraction diagram of α -TaON using Cu- $K\alpha_1$ radiation (bottom) and simulated diffraction diagram (top) on the basis of the ICSD entry number 20321.

Clearly, the differences between the experimental and simulated diffraction diagrams are so large both in terms of intensities and positions that the α -TaON structure must also be questioned on experimental ground provided that the bulk phase was identical with the single crystal. If that is the case α -TaON cannot adopt the experimentally proposed structure by Buslaev et al. if their own diffraction diagram is taken seriously.

5.3.3 Discussion

Electronic structure calculations of different sophistication (pseudopotentials, LAPW, LMTO; LDA & GGA) on β -TaON are in excellent agreement with the experimental results, thereby confirming prior results of de Width et al. [97]. The calculated volumes are very near the experimental volume, and also the calculated bandgaps are surprisingly close to the experimental value of (indirect) 2.4 eV. The analysis of chemical bonding yields the expected result of higher ionicity for Ta–O bonding compared to Ta–N although the latter one turns out to be stronger. In short, electronic structure calculations of DFT type do not pose strong difficulties with respect to energies, spatial parameters etc. despite the significant amount of electronic correlation to be expected in these materials.

The calculated properties of α -TaON, however, do not at all agree with the experimental ones proposed by Buslaev et al. The difference between calculated and experimental volumes — ca. 20% — is simply too large to assume that the error is caused by the approximations of the DFT functional; instead, it questions the experimental structure. Also, the aberration of the experimental molar volume compared to the one of the β -phase is absurdly large. The huge difference in molar volumes is also reflected by a huge difference in the total energies for the optimized structure of the (here questioned) α -TaON and the (well-characterized) β -TaON. Upon approximating enthalpy differences by differences in total electronic energies, the transformation reaction between the two polymorphs would yield



which is extraordinary large for a phase transformation. This huge amount of energy simply indicates that the proposed structure of α -TaON is an extremely high-lying structure alternative on the energy axis; too high to be taken seriously. Finally, a comparison between simulated and experimental XRD patterns clearly shows that the experimentally proposed structure is incompatible with the experimental data given by the authors; until now nobody has published a corresponding observation before. Excluding simple faults in the XRD data handling, the above comparison further supports the used electronic structure

results.

As it seems, α -TaON and its crystal structure have been part of the crystal-chemical literature since 1966 and *have therefore survived the regular checks applied to the digitally stored structure information*; thus, α -TaON is still contained (2005) in the Inorganic Crystal Structure Database (ICSD) under entry number 20321, without any warning sign. The electronic structure calculations together with Buslaev's own diffraction diagram manifest that this entry must be removed from the above database in order not to badly influence secondary data generated from the databases.

5.3.4 Mixed Oxynitrides of Niobium and Tantalum

In the previous section it was shown that the baddeleyite structure is the only stable modification of TaON at ambient conditions. Since NbON adopts the same structure and both pentavalent ions have the same ionic radius $\text{Nb}^{5+}/\text{Ta}^{5+}$: 0.69 Å [84], it should be possible to synthesize mixed oxynitrides containing both tantalum and niobium as well. Similar experiments have already successfully been performed on tantalum and niobium nitrides [106]. In the case of the oxynitrides, this exchange can be interesting due to the possibility of bandgap tuning without changing the anionic sublattice. Remind that NbON is a blue and TaON is a yellow semiconductor whose bandgaps are mainly determined by the nitrogen states at the Fermi level and the transition-metal states at the bottom of the conduction bands. The latter states will of course change when tantalum is substituted by niobium. GGA-pseudopotential calculations were performed on TaON, in which tantalum is substituted by niobium. For the reason of simplicity and computational effort only three different compositions are included and shown in the Table 14. To determine the stability of the mixed compounds, the energy of these compounds is compared with the energy of the simple ternary oxynitrides (TaON, NbON). The energy difference (ΔE) is calculated by:

$$\Delta E = E_{(\text{Ta}_{4-x}\text{Nb}_x\text{O}_4\text{N}_4)} - x \cdot E_{(\text{NbON})} - (4 - x) \cdot E_{(\text{TaON})}. \quad (2)$$

All total energies are negative, therefore a negative value of (ΔE) implies a stabilization of the mixed compound.

Composition	Energy	ΔE
Ta ₄ O ₄ N ₄	-124.12	-
Ta ₃ Nb ₁ O ₄ N ₄	-121.65	-0.02
Ta ₂ Nb ₂ O ₄ N ₄	-119.16	-0.02
Ta ₁ Nb ₃ O ₄ N ₄	-116.66	-0.01
Nb ₄ O ₄ N ₄	-114.16	-

Table 14: Energy of the niobium substituted tantalum oxynitrides in comparison with the simple ternary compounds, TaON and NbON. All energies are in eV. ΔE is calculated relative to the energies of NbON and TaON. (Equation 2)

From the enthalpic point of view the energy gain of mixed oxynitrides is very small. They are even too small to state that one composition is preferred. The configurational entropy, however, will certainly prefer the mixed phases, so they might be experimentally accessible. Within these mixed phases several different cation arrangements are possible. There is, however, no preference for one specific cation order. The cations may be randomly distributed.

The electronic structure of Ta₂Nb₂O₄N₄ is calculated with LMTO and the calculated bandgap is compared with the ones from TaON and NbON. All compounds were assumed to adopt the baddeleyite structure and resemble the preferred anion order from the previous sections. The band structures are shown in Figure 26.

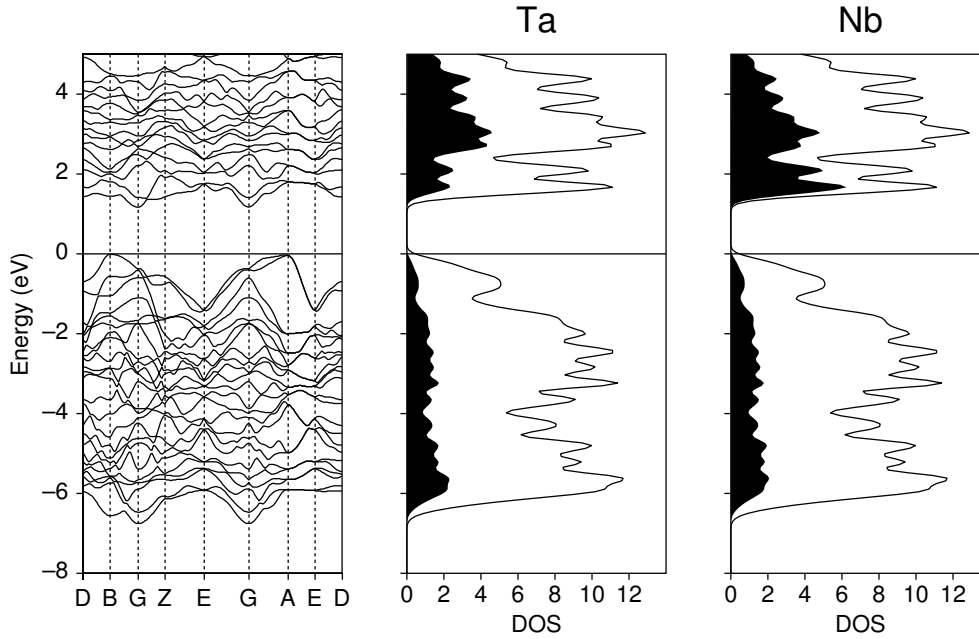


Figure 26: Band structure of $\text{Ta}_2\text{Nb}_2\text{O}_4\text{N}_4$ in the baddeleyite structure on the left and density-of-states with the tantalum projections (middle) and the niobium projections (right).

The calculations result in a direct bandgap of 1.4 eV, which is smaller than the ones of NbON and TaON (see previous sections). One can notice the higher niobium contribution in the density-of-states at about 2 eV, in comparison to the tantalum states, which obviously caused the smaller gap. A smaller bandgap indicates an absorption of larger wavelengths and a corresponding change of color to the energetically higher part of the visible spectrum. A quantitative prediction can not be given here since only ground-state DFT calculations are performed, but it can be said that a significant change in bandgap for TaON can be expected when tantalum is substituted by niobium. This leads to the overall conclusion that niobium doped TaON can be synthesized and will lead to a change in color and therefore can easily be used for bandgap tuning.

5.3.5 High-pressure phases of NbON and TaON

In this section the high-pressure behavior of NbON and TaON is investigated and it will be searched for possible high-pressure phases. Since the chemical

behavior of NbON and TaON is quite similar, the diagrams are referring to TaON for simplicity. Whenever there are explicit differences between NbON and TaON, these are specified in the text.

At the beginning, the search for high-pressure phases of NbON and TaON started with eleven AB_2 structures which have larger coordination numbers than the sevenfold coordination of baddeleyite. Then, all structure types were allowed to adopt TaON and NbON through a minimization of the total energies by means of an independent optimization of the lattice parameters and the atomic sites. The most important types are listed in Table 15. The effective coordination number is calculated after Brunner and Schwarzenbach [107]. A complete list of all calculated types is given in Appendix D. As expected, the baddeleyite

Structure type	ecn	E_0	V_0	ΔE	ΔV	p^*
Baddeleyite	6.5	-31.03	32.31	0	0	
Cotunnite	8.1	-30.25	28.19	0.78	-4.12	30
Fluorite	7.6	-30.11	30.95	0.92	-1.36	108
Bismoclite	8.3	-30.01	27.99	1.02	-4.32	38

Table 15: Structure type, effective coordination number of the tantalum atom (ecn), total energy (E_0) and volume (V_0) at zero pressure, relative energy (ΔE) and relative volume (ΔV) with respect to the lowest energy-configuration for several hypothetical polymorphs of TaON. p^* indicates an approximate transition pressure. Energies are given in eV and volumes in \AA^3 per formula unit TaON, p^* in GPa.

structure turns out as lowest in energy. A pressure-induced phase transition into the cotunnite type is predicted at roughly 30 GPa. Here, the zeroth-order transition pressure ($p^* = -\frac{\partial E}{\partial V}$) serves as a crude approximation which lets us exclude too high-lying structure types but detect plausible ones. Given that a lucrative polymorph is identified, the energy-volume dependence is calculated in detail and plotted by means of an energy-volume diagram (see Figure 27). For reasons of brevity, the (similar) diagram of NbON is not shown. The numerical

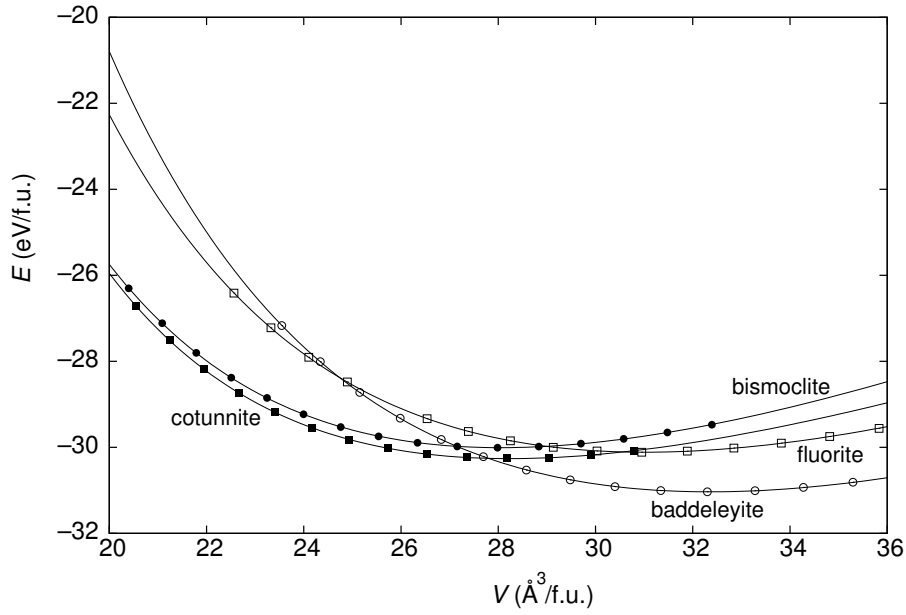


Figure 27: Calculated energy-volume diagram of TaON in different structure types.

data of NbON are slightly different from TaON, reflecting the different atomic natures but still preferring the baddeleyite structure and keeping the energetic ordering. Like in the case of VON, the enthalpy-pressure dependence of TaON in different structure types is calculated. The results for TaON are shown in Figure 28.

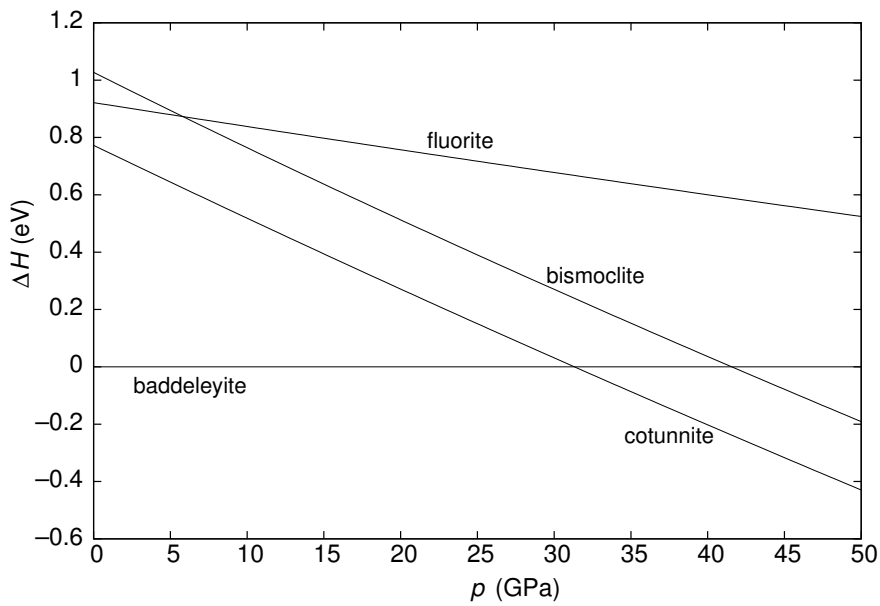


Figure 28: Theoretical enthalpy-pressure diagram of TaON.

At approximately 31 GPa, a phase transformation of TaON from baddeleyite to cotunnite appears. The cotunnite type is characterized by a ninefold coordination of the tantalum atom. The anions form trigonal prisms, capped on all rectangular faces, around the central metal atom, as shown in Figure 29. In the present case, there are four oxygen atoms and five nitrogen atoms bonded to the tantalum with distances of 2.04–2.33 Å.

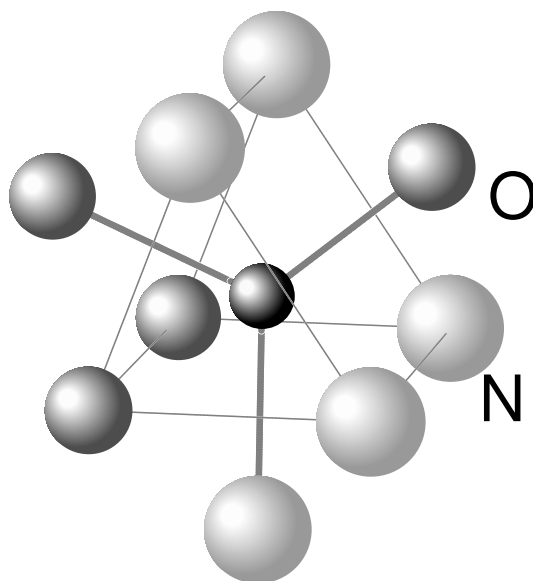


Figure 29: Tantalum coordination in the high-pressure cotunnite structure of TaON, a distorted trigonal prism capped on all rectangular faces.

NbON is also predicted to exhibit almost the same high-pressure behavior as TaON. A pressure-induced phase transition of NbON (baddeleyite) into the cotunnite structure sets in about 27 GPa. Within the cotunnite type, niobium has the same ninefold coordination like tantalum (Figure 29). It is worthwhile studying whether an order of the anions can be found for phases, thus different anion arrangements were calculated within this structure type for NbON as well as for TaON. The energy differences between the several arrangements, however, are tiny (less than 0.04 eV/f.u.). This leads to the conclusion that no specific anion order is preferred within the high-pressure phases of TaON and NbON; both might well be disordered with respect to O and N.

Electronic-structure calculations on TaON in the baddeleyite structure were

first performed by de Widdh *et al.* [97] and extended by this work through a chemical bonding analysis. The latter calculations yield a direct bandgap of 2.1 eV which nicely corresponds to the actual yellow-colored solid. The electronic structure of the cotunnite type of TaON also using LMTO theory and the GGA functional was calculated. The density-of-states and a closer look into the bonding situation of TaON are given in Figure 30.

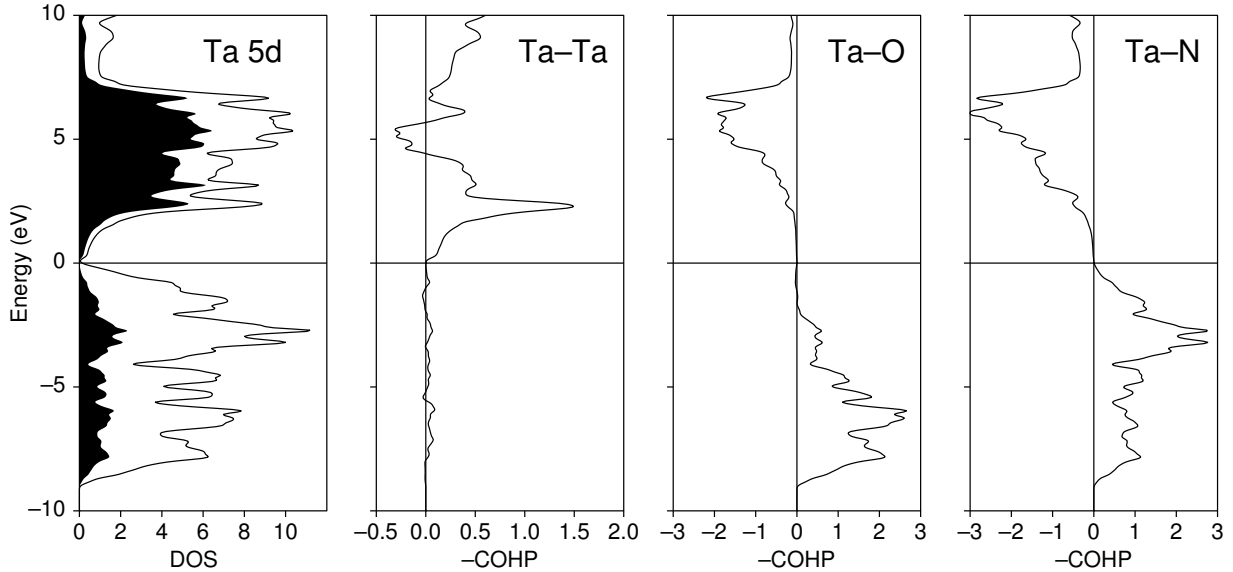


Figure 30: Density-of-states of TaON in the cotunnite structure with local $3d$ projections and Crystal Orbital Hamilton Populations (COHP) for the Ta-Ta, Ta-O and Ta-N interactions.

These calculations predict high-pressure TaON as a semiconductor with a very small bandgap of 0.15 eV. There are strong tantalum-oxygen and tantalum-nitrogen interactions below the Fermi level which stabilize this high-pressure phase. The tantalum-tantalum interactions are small, simply because of the large interatomic distance of 3.10 Å. As expected, the density-of-states and COHP curves of high-pressure NbON look very much the same. One major difference, however, is that NbON is predicted to be a metallic conductor. It is clear that, formally, there is still a pentavalent niobium (Nb^{5+}) but parts of the electronic density formally located in $2p$ states of O and N have been delocalized over the entire structure. Similar transformations of insulating (or semiconduct-

ing) materials into metallic ones have been reported before whenever pressure is applied [108].

5.3.6 Anion order in VON, NbON and TaON

The anion order is one of the main characteristics of an oxynitride compound and therefore a short summation will be given here. The arrangement of the anions plays a major role and is already often discussed in this work. Within the 3d transition-metal oxynitrides, the anions are randomly distributed. On the contrary, the stoichiometric compounds VON, NbON, and TaON show a strict order for the anion arrangements. The relative energies of the different anion arrangements in the baddeleyite structure of VON, NbON and TaON are shown in Table 16. Recall that in the smallest unit cell of the baddeleyite structure, five different anion arrangements are possible.

Position=Occupation	VON	NbON	TaON
A1 = 4 × N	0	0	0
A1 = 3 × N; 1 × O	12.0	16.7	19.2
A1 = 2 × N; 2 × O	17.5	25.2	28.8
A1 = 1 × N; 3 × O	18.4	34.3	41.2
A1 = 4 × O	11.3	32.3	15.7

Table 16: Theoretical relative energies (kJ/mol) as a function of anionic ordering for VON, NbON, and TaON.

All three oxynitrides prefer the same anion order, where the A1 position is occupied only by nitrogen. The relative differences between the anion arrangements decrease when moving from TaON to VON. Until now it is not entirely clear where this specific anion order originates from. Trivially, different anion occupations lead to different total energies, but the composition does not change. This means that in the case of the baddeleyite structure the cations are always surrounded by seven anions. In the lowest-energy configuration the cation is coordinated by four nitrogen and three oxygen atoms. The cation–anion inter-

actions are always strongly bonding (see Figure 22). A different coordination of the cation will consequently not lead to a significant energy gain or loss. On the contrary, the anions are surrounded either by four cations (position A1) or by three cations (position A2). From the electrostatic point of view, the different occupations of the anion positions should lead to a change of the Coulomb part of the lattice energy. These purely electrostatic calculations were performed using the MAPLE (Madelung part of lattice energy) program package [109, 110], assuming ideal ionic charges of +5, -2 and -3 for V, O and N, respectively. Hereby only the attractive Coulomb interactions are taken into account. The calculations were performed for the two extreme cases, where once the A1 position is only occupied with nitrogen ($A1 = 4 \times N$) and once with oxygen ($A1 = 4 \times O$). The MAPLE value for the first case is 87073 kJ/mol and for the second case 84744 kJ/mol. This indicates that in the first case ($A1=4 \times N$) the Coulomb energy is much larger and therefore stabilizes this specific anion arrangement. The large MAPLE value for $A1 = 4 \times N$ scenario is easily explained; only in this particular case is there a maximum number of cations around the most strongly charged (N^{3-}). A substitution of N^{3-} by O^{2-} therefore must result in a lowered Madelung field.

These simple electrostatic calculations explain why one anion order ($A1 = 4 \times N$) is favored over all others. It does not, however, explain why the other ordered phase ($A1 = 4 \times O$) for VON is the second lowest in energy. Therefore the anion-anion interactions (N-N, N-O, and O-O) are studied for the five different anion arrangements from Table 16. The bonding analysis is performed using the COHP technique. The integrated COHP (ICOHP) can be regarded as an indicator of the bond strength. The ICOHPs of the N-N, N-O, and O-O bonds for the five different anion arrangements of VON are calculated and shown in Table 17. The ICOHP values are based on the optimized lattice parameters and atomic positions and the bondlengths in every distribution, apart from minor changes, are almost the same.

Position=Occupation	N-N	N-O	O-O
A1 = 4× N	-0.2004	-0.0262	-0.0106
A1 = 3× N; 1× O	-0.0735	-0.0209	-0.0106
A1 = 2× N; 2× O	-0.0552	-0.0634	-0.0466
A1 = 1× N; 3× O	-0.0245	-0.0296	-0.0272
A1 = 4× O	-0.2697	-0.0128	-0.0065

Table 17: ICOHP values for the N-N, N-O and O-O bonds of VON in the baddeleyite structures for different anion arrangements; energies in eV/bond.

Surprisingly, all anion-anion interactions are slightly bonding reflected by the negative ICOHP values. The ordered phases are the ones where the A1 position is occupied by only one sort of anions (A1 = 4× N and A1 = 4× O). The strongest bonding interactions are found for the N-N bond in these ordered phases. When the anion order is changed (e.g. A1 = 3× N; 1× O), the N-N bond within this new arrangement is much weaker, as can be seen at larger ICOHP values (-0.0735 eV/bond). The other bonds (N-O and O-O) are less sensitive with respect to such an exchange. Qualitatively, these results are in good agreement with the total energies from Table 16, where the ordered phases are also preferred over the disordered ones. The much stronger cation-anion interactions, however, play a more decisive role in the preference for one specific anion order. In this case, the anion-anion interactions only support this preference. It can generally be said that if the anion positions are coordinated by a different number of cations, the cation-anion interactions will determine whether there is a specific anion order or not. If the anion positions are equally coordinated, the anion-anion interactions become more important.

6. Summary

In this work the chemical properties of oxynitrides of transition metals are investigated. These investigations are performed on a theoretical basis using first-principles calculations. First, the research was focused on the $3d$ transition-metal oxynitrides (Sc–Ni) where the structural properties of only $\text{CoO}_{0.5}\text{N}_{0.5}$, $\text{VO}_{0.5}\text{N}_{0.5}$ and $\text{CrO}_{0.5}\text{N}_{0.5}$ are known. These experimental results could be perfectly reproduced. Moreover, the structural properties of the other oxynitrides are predicted. The structure changes from the rocksalt structure for the early $3d$ transition-metal oxynitrides (Sc–Mn) to the zinc blende structure for the later ones (Fe–Ni). This phenomenon can be explained in a qualitative way by a detailed chemical bonding analysis with use of the COHP technique. It shows that for a higher electron count the Fermi level lies in the metal–metal antibonding region of the COHP for the rocksalt structure and therefore destabilizes this structure type. The structure changes to the zinc blende where these metal–metal antibonding interactions are less pronounced. Supercell calculations on some of these $3d$ transition-metal oxynitrides revealed no pronounced preference for one specific anion order, even randomly distributed nitrogen and oxygen atoms are favored. Furthermore, it is this random anion arrangement which annihilates the magnetic moments on the metal atom in the case of $\text{CoO}_{0.5}\text{N}_{0.5}$. For this reason, all the oxynitrides containing ferromagnetic metals (Fe, Co and Ni) are predicted as being nonmagnetic. The search for magnetic transition-metal oxynitrides should be focused on $\text{MnO}_{0.5}\text{N}_{0.5}$, where the calculated energy difference between the nonmagnetic and ferromagnetic state is large enough to withstand the influence of the anion distribution. Although a disordered anion arrangement will entropically stabilize the oxynitride, all the oxynitrides remain metastable with respect to the corresponding oxides and nitrides. This of course,

complicates the synthesis of a $3d$ transition metal enormously.

Second, the stoichiometric oxynitrides of the fifth-group are investigated. Until now there is no report about any stoichiometric vanadium oxynitride (VON). A high-pressure synthesis of VON is proposed, starting from V_2O_5 , VN and N_2 . It should be accessible at pressures beyond 12 GPa where VON adopts the baddeleyite structure and is a small band gap semiconductor (0.6 eV). This is in good agreement with the pressure-homologue rule of Neuhaus; VON is waiting for its discovery.

Within the literature there exist two possible phases of TaON, which is one of the most investigated transition-metal oxynitrides. One phase adopts the baddeleyite structure and the other has a complicated hexagonal structure. The calculated results of TaON in the baddeleyite structure match almost perfectly with the experimental data. The hexagonal structure, however, distorts during the relaxation of the lattice parameters and the atomic positions. A detailed investigation of this phase showed that TaON cannot exist in this structure and should therefore be erased from any crystal structure databases. Niobium oxynitride also exhibits the baddeleyite structure, but is less investigated as TaON. The experimental lattice parameters and atomic sites could be very well reproduced. For the first time the electronic structure of NbON in the baddeleyite structure is calculated and results in a band gap of 1.7 eV, which nicely corresponds to the actual blue-colored semiconductor. Electronic structure calculations on mixed tantalum and niobium containing oxynitrides show a decrease of the band gap. Since our theoretical methods are limited to the ground state, only a qualitative interpretation is allowed here. But it can be said that niobium doped TaON will change its color and therefore may be easily used for band gap tuning, without changing the anionic sublattice.

A pressure-induced phase transition of NbON and TaON is suggested to happen at 27 and 31 GPa respectively. The structure changes from baddeleyite to cotunnite, which goes together with an increase of the coordination number of the metal atom. Electronic structure calculations of TaON in the cotunnite structure result in a very small band gap of 0.15 eV, NbON is even predicted to be a metal. Within these high-pressure phases of TaON and NbON, no spe-

cific anion order is preferred, both might well be disordered with respect to O and N. On the contrary these oxynitrides prefer one specific anion order when they exhibit the baddeleyite structure. The reason is found in the cation–anion interactions for this structure type. The anion–anion interactions play a minor role.

Overall it can be said that this work answers a few questions of the broad field of research of the transition-metal oxynitrides and it hopefully assists to find an appropriate synthesis of some of the calculated oxynitrides.

Bibliography

- [1] R. MARCHAND, Y. LAURENT, J. GUYADER, P. L'HARIDON, and P. VERDIER, *J. Eur. Ceram. Soc.* **8**, 197 (1991).
- [2] K. MIGA, K. STANCZYK, C. SAYAG, D. BRODZKI, and G. DJÉGA-MARIADASSOU, *J. Cat.* **183**, 63 (1999).
- [3] G. HITOKI, T. TAKATA, J. KONDO, M. HARA, H. KOBAYASHI, and K. DOMEN, *Chem. Comm.* **16**, 1698 (2002).
- [4] M. JANSEN and H. LETSCHERT, *Nature* **404**, 980 (2000).
- [5] R. ROBERT and R. AGUIAR, *Workshop Rauischholzhausen* (2005).
- [6] *ICSD, Inorganic Crystal Structure Database*, National Institute of Standards and Technology (NIST) and Fachinformationszentrum Karlsruhe (FIZ), Version 2004-02.
- [7] I. NEWTON, *Philosophiae Naturalis Principia Mathematica*, London, 1687.
- [8] D. KLEPPNER, *Rev. Mod. Phys.* **71**, 78 (1999).
- [9] E. SCHRÖDINGER, *Nobel Lecture* (1933).
- [10] L. H. THOMAS, *Proc. Cambridge Phil. Soc.* **23**, 542 (1928).
- [11] E. FERMI, *Z. Physik* **48**, 73 (1928).
- [12] J. C. SLATER, *Phys. Rev.* **81**, 385 (1951).
- [13] P. HOHENBERG and W. KOHN, *Phys. Rev. B* **136**, 864 (1964).

-
- [14] W. KOHN and L. J. SHAM, *Phys. Rev. A* **137**, 1697 (1965).
- [15] U. VON BARTH and L. HEDIN, *J. Phys. C* **5**, 1629 (1972).
- [16] J. P. PERDEW, *Electronic Structure of Solids '91*, P. Ziesche, H. Eschrig, Akademie Verlag, Berlin, 1991.
- [17] G. KRESSE and J. HAFNER, *Phys. Rev. B* **47**, 558 (1993).
- [18] G. KRESSE and J. HAFNER, *Phys. Rev. B* **49**, 14251 (1994).
- [19] G. KRESSE and J. FURTHMÜLLER, *Phys. Rev. B* **55**, 11169 (1996).
- [20] G. KRESSE and J. FURTHMÜLLER, *Comput. Mat. Sci.* **6**, 15 (1996).
- [21] G. KRESSE and J. HAFNER, *J. Phys.: Condens. Matt.* **6**, 8245 (1994).
- [22] G. KRESSE and D. JOUBERT, *Phys. Rev. B* **59**, 1758 (1999).
- [23] J. C. SLATER, *Phys. Rev.* **51**, 151 (1937).
- [24] J. KORRINGA, *Physica* **13**, 392 (1947).
- [25] W. KOHN and N. ROSTOKER, *Phys. Rev. B* **136**, 1111 (1964).
- [26] O. K. ANDERSEN, *Computational Methods in Band Theory*, Plenum, New York, 1971.
- [27] R. DRONSKOWSKI, *Computational Chemistry of Solid State Materials*, Wiley-VCH, Weinheim, New York, 2005.
- [28] O. K. ANDERSEN, *Phys. Rev. B* **12**, 3060 (1991).
- [29] P. BLAHA, K. SCHWARZ, G. MADSEN, D. KVASNICKA, and J. LUITZ, *WIEN2K, An augmented Plane Wave + Local Orbitals Program for Calculating Crystal Properties* (1999).
- [30] G. KRIER, O. JEPSEN, A. BURKHARDT, and O. K. ANDERSEN, *Programm TB-LMTO-ASA Version 4.7*, Stuttgart.
- [31] R. DRONSKOWSKI and P. E. BLÖCHL, *J. Phys. Chem.* **97**, 8617 (1993).

- [32] T. HUGHBANKS and R. HOFFMANN, *J. Am. Chem. Soc.* **105**, 3528 (1983).
- [33] G. A. LANDRUM and R. DRONSKOWSKI, *Angew. Chem.* **112**, 1598 (2000).
- [34] B. ECK, R. DRONSKOWSKI, M. TAKAHASHI, and S. KIKKAWA, *J. Mater. Chem.* **9**, 1527 (1999).
- [35] Y. KURTULUS and R. DRONSKOWSKI, *J. Solid State Chem.* **176**, 390 (2003).
- [36] V. DUFEK, F. PETRU, and V. BROZEK, *Monatsh. Chemie* **98**, 2424 (1967).
- [37] V. DUFEK, F. PETRU, and V. BROZEK, *Monatsh. Chemie* **100**, 1628 (1969).
- [38] D. TAYLOR, *Trans. J. Brit. Ceram. Soc.* **83**, 5 (1984).
- [39] G. BRAUER and H. REUTHER, *Z. Anorg. Allg. Chem.* **395**, 151 (1973).
- [40] S. SASAKI, K. FUJINO, Y. TAKEUCHI, and R. SADANAGA, *Acta Crystallogr. A* **36**, 904 (1980).
- [41] S. SASAKI, K. FUJINO, Y. TAKEUCHI, and R. SADANAGA, *J. Phys. Chem. Solids* **53**, 141 (1992).
- [42] H. FJELLVAG, F. GROENVOLD, S. STOELLEN, and B. C. HAUBACK, *J. Solid State Chem.* **124**, 52 (1996).
- [43] M. R. DANIEL and A. P. CRACKNELL, *Phys. Rev.* **177**, 932 (1969).
- [44] D. ARMYTAGE and B. E. FENDER, *Acta Crystallogr. B* **30**, 809 (1974).
- [45] I. I. MAZIN and V. I. ANISIMOV, *Phys. Rev. B* **55**, 12822 (1997).
- [46] J. HÄGLUND, G. GRIMVALL, T. JARLBORG, and A. F. GUILLERMET, *Phys. Rev. B* **43**, 14400 (1991).

- [47] T. C. LEUNG, C. T. CHAN, and B. N. HARMON, *Phys. Rev. B* **44**, 2923 (1991).
- [48] P. DUFEK, P. BLAHA, V. SLIWKO, and K. SCHWARZ, *Phys. Rev. B* **49**, 10170 (1997).
- [49] K. TERAOKURA, T. OGUCHI, A. R. WILLIAMS, and J. KÜBLER, *Phys. Rev. B* **30**, 4734 (1984).
- [50] V. L. ANISIMOV, J. ZAAANEN, and O. K. ANDERSEN, *Phys. Rev. B* **44**, 943 (1991).
- [51] M. J. REDMAN and E. G. STEWARD, *Nature* **198**, 867 (1962).
- [52] R. W. GRIMES and K. P. D. LAGERLÖF, *J. Am. Ceram. Soc.* **74**, 270 (1991).
- [53] D. R. LIDE, *CRC Handbook of Chemistry and Physics, 86th Edition*, 2005.
- [54] B. HAJEK, V. BROZEK, and P. DUVIGNEAUD, *J. Less-Common Met.* **33**, 385 (1973).
- [55] R. NIEWA, D. A. ZHEREBTSOV, M. KIRCHNER, M. SCHMIDT, and W. SCHNELLE, *Chem. Mater.* **16**, 5445 (2004).
- [56] S. NAGAKURA, T. KUSUNOKI, F. KAKIMOTO, and Y. HIROTSU, *J. Appl. Crystallogr.* **8**, 65 (1975).
- [57] L. CORLISS, N. ELLIOT, and J. HASTINGS, *Phys. Rev.* **117**, 929 (1960).
- [58] A. FILIPPETTI and N. HILL, *Phys. Rev. Lett.* **85**, 5166 (2000).
- [59] B. SAHU and L. KLEINMAN, *Phys. Rev. B* **68**, 113101 (2003).
- [60] K. SUZUKI, Y. YAMAGUCHI, T. KANEKO, H. YOSHIDA, Y. OBI, H. FUJIMORI, and H. MORITA, *J. Phys. Soc. Jpn.* **70**, 1084 (2001).
- [61] K. SUZUKI, T. KANEKO, H. YOSHIDA, Y. OBI, H. FUJIMORE, and H. MORITA, *J. Alloys Compd.* **306**, 66 (2000).

- [62] K. SUZUKI, H. MORITA, T. KANEKO, H. YOSHIDA, and H. FUJIMORI, *J. Alloys Compd.* **201**, 11 (1993).
- [63] K. SUZUKI, T. KANEKO, H. YOSHIDA, H. MORITA, and H. FUJIMORI, *J. Alloys Compd.* **224**, 232 (1995).
- [64] H. NAKAGAWA, S. NASU, H. FUJI, M. TAKAHASHI, and F. KANAMARU, *Hyperfine Interact.* **69**, 455 (1991).
- [65] O. SCHMITZ-DUMONT and N. KRON, *Angew. Chem.* **67**, 231 (1955).
- [66] K. SUZUKI, T. SHINOHARA, F. WAGATSUMA, T. KANEKO, H. YOSHIDA, Y. OBI, and S. TOMIYOSHI, *J. Phys. Soc. Jpn.* **72**, 1175 (2003).
- [67] G. BRAUER and J. R. WEIDLEIN, *Angew. Chem. Int. Ed. Engl.* **4**, 10 (1965).
- [68] G. BRAUER, J. R. WEIDLEIN, and J. STRÄHLE, *Z. Anorg. Allg. Chem.* **348**, 298 (1962).
- [69] J. C. GILLES and R. COLLONGUES, *C. R. Acad. Sci.* **254**, 1084 (1962).
- [70] N. R. CRAWFORD, J. S. KNUTSEN, G. H. K. A. YANG, S. MCKERNAN, F. B. MCCORMICK, and W. L. GLADFELTER, *Chem. Vap. Dep.* **4**, 181 (1998).
- [71] G. BRAUER and H. REUTHER, *Z. Anorg. Allg. Chem.* **395**, 151 (1973).
- [72] T. SUZUKI, H. SAITO, M. HIRAI, H. SUEMATSU, W. JIANG, and K. YATSUI, *Thin Solid Films* **407**, 118 (2002).
- [73] P. WILHARTITZ, S. DREER, and P. RAMMINGER, *Thin Solid Films* **447**, 289 (2004).
- [74] M.-W. LUMEY and R. DRONSKOWSKI, *Adv. Funct. Mater.* **14**, 371 (2004).
- [75] S. PRADHAN and P. REUCROFT, *J. Cryst. Growth* **250**, 588 (2003).
- [76] P. SCHMIDT, *Z. Anorg. Allg. Chem.* **628**, 2191 (2002).

- [77] P. KROLL and M. MILKO, *Z. Anorg. Allg. Chem.* **629**, 1737 (2003).
- [78] T. BREDOW and M. LERCH, *Z. Anorg. Allg. Chem.* **630**, 2262 (2004).
- [79] B. WANG, B. C. CHAKOUMAKOS, B. C. SALES, and J. B. BATES, *J. Solid State Chem.* **122**, 376 (1996).
- [80] C. KITTEL, *Introduction to Solid State Physics*, Wiley, New York, 1966.
- [81] J. A. A. KETELAAR, *Nature* **137**, 316 (1936).
- [82] J. M. COCCIANTELLI, P. GRAVEREAU, J. P. DOUMERC, M. POUCHARD, and P. HAGENMULLER, *J. Solid State Chem.* **93**, 497 (1991).
- [83] P. KROLL, *private communication Aachen* (2004).
- [84] R. D. SHANNON, *Acta Crystallogr. A* **32**, 751 (1976).
- [85] A. NEUHAUS, *Chimia* **18**, 93 (1964).
- [86] G. AUFFERMANN, Y. PROTS, and R. KNIEP, *Angew. Chem.* **113**, 565 (2001).
- [87] G. V. VAJENINE, G. AUFFERMANN, Y. PROTS, W. SCHNELLE, R. K. KREMER, A. SIMON, and R. KNIEP, *Inorg. Chem.* **40**, 4866 (2001).
- [88] N. SCHÖNBERG, *Acta Chem. Scand.* **8**, 208 (1954).
- [89] G. BRAUER, *J. Less-Common Met.* **2**, 131 (1960).
- [90] G. BRAUER and R. ESSELBORN, *Z. Anorg. Allg. Chem.* **308**, 52 (1961).
- [91] V. SCHWARTZ and S. T. OYAMA, *Chem. Mater.* **9**, 3052 (1997).
- [92] K. YAMADA, H. MASUDA, N. SATO, and T. FUJINO, *J. Solid State Chem.* **150**, 36 (2000).
- [93] D. ARMYTAGE and B. E. F. FENDER, *Acta Crystallogr. B* **30**, 809 (1974).
- [94] N. SCHÖNBERG, *Acta Chem. Scand.* **8**, 620 (1954).

- [95] Y. A. BUSLAEV, M. A. GLUSHOVA, M. M. ERSHOVA, and E. M. SHUSTOROVICH, *Neorg. Mater.* **2**, 2120 (1966).
- [96] N. E. BRESE and M. O'KEEFFE, *Structure and Bonding* **79**, 309 (1992).
- [97] C. M. FANG, E. ORHAN, G. A. DE WIJS, H. T. HINTZEN, R. A. DE GROOT, R. MARCHAND, J. Y. SAILLARD, and G. DE WITH, *J. Mater. Chem.* **11**, 1248 (2001).
- [98] M.-W. LUMEY and R. DRONSKOWSKI, *Z. Anorg. Allg. Chem.* **629**, 2173 (2003).
- [99] E. ORHAN, F. TESSIER, and R. MARCHAND, *Sol. Stat. Sci.* **4**, 1071 (2002).
- [100] Y. A. BUSLAEV, G. M. SAFRONOV, V. I. PAKHOMOV, M. A. GLUSHOVA, V. P. REPKO, M. M. ERSHOVA, A. N. ZHUKOV, and T. A. ZHDANOVA, *Neorg. Mater.* **5**, 45 (1969).
- [101] M. WEISHAUPT and J. STRÄHLE, *Z. Anorg. Allg. Chem.* **429**, 261 (1977).
- [102] G. KUNZE, *Z. Kristallogr.* **110**, 282 (1958).
- [103] N. SCHÖNBERG, *Acta Chem. Scand.* **8**, 199 (1954).
- [104] R. O. JONES and O. GUNNARSSON, *Rev. Mod. Phys.* **61**, 689 (1989).
- [105] W. KRAUS and G. NOLZE, *PowderCell, Version 2.4*, Federal Institute for Materials Research and Testing, Berlin.
- [106] G. BRAUER and W. KILIANI, *Z. Anorg. Allg. Chem.* **452**, 17 (1979).
- [107] G. O. BRUNNER and D. SCHWARZENBACH, *Z. Kristallogr.* **133**, 127 (1971).
- [108] H. G. DRICKAMER and C. W. FRANK, *Electronic Transitions and the High Pressure Chemistry and Physics of Solids*, Chapman and Hall, London, 1973.
- [109] R. HOPPE, *Angew. Chem.* **78**, 52 (1966).

-
- [110] R. HOPPE, *Angew. Chem.* **82**, 7 (1970).
- [111] S. H. VOSKO, L. WILK, and M. NUSAIR, *Can. J. Phys.* **58**, 1200 (1980).
- [112] J. P. PERDEW, S. BURKE, and M. ERNZERHOF, *Phys. Rev. Lett.* **77**, 3865 (1996).
- [113] D. VANDERBILT, *Phys. Rev. B* **41**, 7892 (1990).
- [114] J. VON APPEN and M.-W. LUMEY, *Lumpen 3.1*, Aachen, 2004.
- [115] B. ECK, *wxDragon 1.2.5c*, Aachen, 1994–2005.

A. Technical Details

A.1 LMTO

The program used was TB-LMTO-ASA 4.7 [30]. Effects of exchange and correlation were treated in the local density approximation (LDA) as parameterized by Vosko, Wilk and Nusair [111], augmented by the gradient-based corrections of Perdew and Wang (GGA) [16]. All results rely on well-converged structures with respect to the k -point sampling. The number of irreducible k -points was about 300–2500, depending on the investigated system. The iterative procedure was stopped when an energy convergence of 10^{-5} Ry was reached. LMTO was mostly used for electronic structure calculations and COHP bonding analysis.

A.2 Wien2k

The required input files were prepared with the use of w2web, the fully web-enabled interface to Wien2k. Within this full-potential method the GGA functional, parameterized by Perdew, Burke and Ernzerhof [112] was always used. Convergence of the total energy (10^{-4} Ry) with respect to the plane-wave expansion parameter $R_{\text{MT}}K_{\text{max}}$ and the k -point sampling was checked. A $R_{\text{MT}}K_{\text{max}}$ value of 9 turned out to be sufficient for the accuracy of the calculated total energy.

A.3 VASP

The Vienna *ab initio* Simulation Package (VASP) was used for relaxation of structures, calculation of bulk moduli, high-pressure phases and synthesis. If not

explicitly mentioned, the exchange and correlation was treated in the generalized gradient approximation [16] and the interaction between the ions and the electrons was described by ultra-soft Vanderbilt pseudopotentials [113]. The electronic as well as the ionic ground state was calculated using the conjugate gradient optimization routine until the residual force was smaller than 5×10^{-3} eV/Å. Again all results rely on well-converged structures with respect to cut-off energy (500 eV) and k -point sampling. High-pressure calculations were achieved by manually decreasing the volume of an unit cell. The unit cell was allowed to relax its lattice parameters and atomic sites, but within the constraints of its symmetry and the pre-set volume, to maintain the external pressure. This was done for several steps ($-10\% - +10\%$) leading to an energy-volume plot, from which an enthalpy-pressure diagram can be calculated by Lumpen 3.1 [114], a script generated for easily fitting $E - V$ data with a Murnaghan or Birch-fit.

A.4 wxDragon

The input files of the used programs were either generated or checked by one of the best visualization programs in theoretical chemistry; wxDragon [115]. Also all pictures of geometric (unit cells, atoms) and electronic (bandstructure, DOS and COHP) were visualized by wxDragon and exported as postscript.

B. Crystal Data

Table 18: Experimental and calculated properties of 3d transition-metal nitrides (above) and oxides (below).

Compound	structure type (space group)	experimental		theoretical	
		a [Å]	magnet.	a [Å]	magnet.
ScN	NaCl ($Fm\bar{3}m$)	4.44-4.51 [55]	-	4.54	0
TiN	NaCl ($Fm\bar{3}m$)	4.22-4.24 [56]	-	4.26	0
VN	NaCl ($Fm\bar{3}m$)	4.13-4.15 [39, 80]	-	4.13	0
CrN	NaCl ^d ($Pnma$)	$a = 5.76; b = 2.96$ $c = 4.13$ [57]	AFM	$a = 5.74; b = 3.00$ $c = 4.12$	AFM
MnN	NaCl ^d	$a = 4.26; c = 4.19$ [60]	AFM	$a = 4.22; c = 4.13$	AFM
FeN	ZnS ($F4\bar{3}m$)	4.31 [62]	-	4.24	0
CoN	ZnS ($F4\bar{3}m$)	4.30 [63]	-	4.26	0
NiN	ZnS ($F4\bar{3}m$)	-	-	4.34	0

ScO	NaCl ($Fm\bar{3}m$)	4.54 [36, 37]	-	4.52	0
TiO	NaCl ($Fm\bar{3}m$)	4.18 [38]	-	4.29	0
VO	NaCl ($Fm\bar{3}m$)	4.07 [39, 80]	-	4.13	0
CrO	NaCl ($Fm\bar{3}m$)	-	-	$a = 4.43; b = 4.23$	AFM
MnO	NaCl ($Fm\bar{3}m$)	4.45 [40, 41]	AFM	4.45	AFM
FeO	NaCl ($Fm\bar{3}m$)	4.33 [42]	AFM	4.29	AFM
CoO	NaCl ($Fm\bar{3}m$)	4.25 [43, 51]	AFM	4.23	AFM
NiO	NaCl ($Fm\bar{3}m$)	4.19 [38]	AFM	4.20	AFM

C. Results on VON

Table 19: Structure type, coordination number of the vanadium atom (cn), total energy (E_0) and volume (V_0) at zero pressure, relative energy (ΔE) and relative volume (ΔV) with respect to the lowest-energy configuration for several hypothetical polymorphs of VON. Energies are given in eV and volumes in \AA^3 per formula unit VON.

Structure type	cn	E_0	V_0	ΔE	ΔV
α -Cristobalite	4	-26.209	68.35	0	0
β -Trydimite	4	-26.206	68.36	0.003	0.01
α -ZnCl ₂	4	-26.206	68.38	0.003	0.03
α -Quartz	4	-26.153	55.22	0.056	-13.13
β -Quartz	4	-26.150	55.21	0.059	-13.14
PbCl ₂	4	-26.098	45.73	0.111	-22.62
β -Cristobalite	4	-26.093	68.96	0.116	0.61
β -ZnCl ₂	4	-26.091	68.96	0.118	0.61
Anatase	6	-26.063	32.85	0.146	-35.50
PbO ₂	6	-26.000	34.38	0.209	-33.97
TeO ₂	6	-25.980	31.55	0.229	-36.80
VO ₂	6	-25.980	31.55	0.229	-36.80
Baddeleyite	7	-25.977	27.62	0.232	-40.73
CaCl ₂	6	-25.914	32.02	0.295	-36.33
Rutile	6	-25.913	31.78	0.296	-36.57
Brookite	6	-25.911	31.78	0.298	-36.57
FeOCl	6	-25.884	36.37	0.325	-31.98

Structure type	cn	E_0	V_0	ΔE	ΔV
ZrO ₂ (Orthorh.)	6	-25.880	32.81	0.329	-35.54
ZrO ₂ (Tetragon.)	6	-25.837	37.53	0.372	-30.82
HgCl ₂	5	-25.845	43.39	0.364	-24.96
AlO(OH)	6	-25.817	33.04	0.392	-35.31
ZnO(OH)	6	-25.787	47.76	0.422	-20.59
Cu(OH)Cl	6	-25.773	40.39	0.436	-27.96
FeO(OH)	6	-25.735	38.70	0.474	-29.65
CaCl ₂	6	-25.748	30.51	0.461	-37.84
Cu ₂ O	4	-25.706	30.90	0.503	-37.45
HgI ₂	4	-25.656	49.55	0.553	-18.8
CdCl ₂	6	-25.602	39.14	0.607	-29.21
HgBr ₂	6	-25.601	39.20	0.608	-29.15
CdI ₂	6	-25.600	38.16	0.609	-30.19
SiS ₂	4	-25.394	48.38	0.815	-19.97
EuOF	7	-25.390	28.29	0.819	-40.06
ZrOS	7	-25.303	28.89	0.906	-39.46
CdI ₂	6	-25.148	39.12	1.061	-29.23
TaS ₂	6	-25.145	37.83	1.064	-30.52
MoS ₂	6	-25.143	34.34	1.066	-34.01
PbFCl	8	-24.808	27.11	1.401	-41.24
Fluorite	8	-24.806	27.10	1.403	-41.25
PbFCl	9	-24.603	27.17	1.606	-41.18
AlB ₂	12	-20.838	25.22	5.371	-43.13

D. Results on high-pressure phases of TaON

Table 20: Structure type, effective coordination number of the tantalum atom (ecn), total energy (E_0) and volume (V_0) at zero pressure, relative energy (ΔE) and relative volume (ΔV) with respect to the lowest energy-configuration for several hypothetical polymorphs of TaON. p^* indicates an approximate transition pressure. Energies are given in eV, the volumes in \AA^3 per formula unit TaON and the transition pressure p^* in GPa.

Structure type	ecn	E_0	V_0	ΔE	ΔV	p^*
Baddeleyite	6.5	-31.03	32.31	0	0	
ZrO ₂ (Orthorh.)	2× 6.2, 2× 6.5	-30.45	31.62	0.58	-0.69	134
ZrO ₂ (Tetragon.)	7.1	-30.33	32.24	0.70	-0.07	1600
Cotunnite	8.1	-30.25	28.19	0.78	-4.12	30
ZrNCl	-	-30.14	43.76	0.89	11.45	-
Fluorite	7.6	-30.11	30.95	0.92	-1.36	108
YOF	8.0	-30.09	30.77	0.94	-1.54	98
Bismoclite	8.3	-30.01	27.99	1.02	-4.32	38
PbFCl	8.0	-29.98	30.78	1.05	-1.53	110
LaSeF	12.0	-25.16	27.89	5.87	-4.42	213
AlB ₂	12.0	-24.87	28.16	6.16	-4.15	238

Danksagung

Meinem Doktorvater, Herrn Prof. Dr. Richard Dronskowski, danke ich für die Einführung in das interessante Gebiet der theoretischen Festkörperchemie. Besonders danke ich ihm für seine Geduld und Streben mich an sein Wissen teilzuhaben.

Herrn Prof. Dr. Ulrich Simon danke ich für die freundliche Übernahme des Korreferats.

Insbesondere möchte ich mich bei meinen Mitstreitern aus der Theorie, Bernhard Eck, Yasemin Kurtulus, Holger Wolff, Michael Gilleßen, Peter Kroll und Jörg von Appen, für die freundschaftliche Zusammenarbeit und hilfreiche Diskussionen bedanken.

Bedanken möchte ich mich bei allen Mitarbeitern des Arbeitskreises Dronskowski, für die angenehme Arbeitsatmosphäre und tatkräftige Unterstützung bei anfallenden Problemen.

Für die kritische Durchsicht des Manuskripts möchte ich mich ganz herzlich bei Mona Marquardt, Bernhard Eck und Jörg von Appen bedanken.

Marciano and Louis, thank you for your loyal service.

Ik wil me ook heel hartelijk bij mijn ouders bedanken, zonder wiens hulp mijn studie scheikunde niet mogelijk zou zijn geweest.

En tot slot wil ik me bedanken bij mijn vrouw Peggy en mijn dochter Anna, voor hun steun en toeverlaat.

Lebenslauf

Persönliche Angaben

Name: Marck-Willem Lumey
Geburtstag: 16.08.1974
Geburtsort: Heerlen (NL)
Familienstand: verheiratet, eine Tochter

Schulbildung

1980–1986 Basisschool "De Cathabel" Lemiers
1986–1992 Atheneum "Sophianum" Gulpen

Studium

1992 Beginn des Chemiestudiums an der RWTH Aachen
1996 Vordiplom
2000 Diplomchemiker-Hauptprüfung
2001 Diplomarbeit bei Prof. Dr. J. Fleischauer am Institut für Organische Chemie der RWTH Aachen
2001–2005 Dissertation unter Anleitung von Prof. Dr. R. Dronskowski am Institut für Anorganische Chemie der RWTH Aachen, Anstellung als wissenschaftlicher Angestellter